Experimental Study of Pressure and Main Gas Ingestion Distributions in a Model Rotor-Stator Disk Cavity

by

Jayanth kumar Thiagarajan

A Thesis Presented in Partial Fulfillment
of the Requirements for the Degree
Master of Science

Approved February 2013 by the
Graduate Supervisory Committee:

Ramendra P. Roy, Chair
Taewoo Lee
Marc Mignolet

ARIZONA STATE UNIVERSITY

May 2013

ABSTRACT

Ingestion of high temperature mainstream gas into the rotor-stator cavities of a gas turbine is one of the major problems faced by the turbine designers. The ingested gas heats up rotor disks and induces higher thermal stresses on them, giving rise to durability concern. Ingestion is usually reduced by installing seals on the rotor and stator rims and by purging the disk cavity by secondary air bled from the compressor discharge. The geometry of the rim seals and the secondary air flow rate, together, influence the amount of gas that gets ingested into the cavities. Since the amount of secondary air bled off has a negative effect on the gas turbine thermal efficiency, one goal is to use the least possible amount of secondary air. This requires a good understanding of the flow and ingestion fields within a disk cavity.

In the present study, the mainstream gas ingestion phenomenon has been experimentally studied in a model single-stage axial flow gas turbine. The turbine stage featured vanes and blades, and rim seals on both the rotor and stator. Additionally, the disk cavity contained a labyrinth seal radially inboard which effectively divided the cavity into a *rim cavity* and an *inner cavity*.

Time-average static pressure measurements were obtained at various radial positions within the disk cavity, and in the mainstream gas path at three axial locations at the outer shroud spread circumferentially over two vane pitches. The time-average static pressure in the main gas path exhibited a periodic

asymmetry following the vane pitch whose amplitude diminished with increasing distance from the vane trailing edge. The static pressure distribution increased with the secondary air flow rate within the inner cavity but was found to be almost independent of it in the rim cavity.

Tracer gas (CO_2) concentration measurements were conducted to determine the sealing effectiveness of the rim seals against main gas ingestion. For the rim cavity, the sealing effectiveness increased with the secondary air flow rate. Within the inner cavity however, this trend reversed –this may have been due to the presence of rotating low-pressure flow structures inboard of the labyrinth seal.

ACKNOWLEDGMENTS

I sincerely thank Professor Ramendra P. Roy for his constant guidance and encouragement. I thank Professor Taewoo Lee and Professor Marc Mignolet for agreeing to be on my committee. I also would like to thank my colleague Parag S. Pathak for his contribution to this work through his selfless involvement and helpful discussions.

Many thanks to past members of the Heat transfer Lab, in particular, Jagdish Balasubramanian and Nihal Junnarkar for their invaluable source of help and guidance. Special thanks to the personnel of the Engineering Technical Services, Dennis Golabiewski and Martin Johnson for their help in putting together various assemblies and design insights.

Thanks are due to my parents and friends for their support and help.

TABLE OF CONTENTS

Page

CHAPTER Page

LIST OF TABLES

LIST OF FIGURES

FIGURE PAGE

NOMENCLATURE

b	outer radius of disk cavity
C	tracer (CO_2) gas concentration
C_{vax}	vane axial chord length
c_w	non-dimensional mass flow rate of purge air, $= \frac{\dot{m}_{purge}}{\mu b}$
$c_{w,fd}$	non-dimensional free disk pumping flow rate, $= 0.219 Re_{\Phi}^{0.8}$
$\dot{m}_{purge}$	mass flow rate of purge air (kg/s)
p	instantaneous static gage pressure
$\bar{p}$	time-average static gage pressure
p_{amb}	ambient pressure
Re_{vax}	main air flow Reynolds number, $= \rho V_{ax} C_{vax} / \mu$
Re_{Φ}	disk rotational Reynolds number, $= \rho \Omega b^2 / \mu$
s	axial gap between rotor and stator disks
V_{ax}	mixed-mean axial velocity of main air in annulus
β_2	angle, to axial direction downstream, of the main air velocity relative to the blade – at just downstream of vane trailing edge (^{o})
η	local sealing effectiveness
μ	dynamic viscosity (kg/m/s)

ρ	density of air (kg/m^3)
Ω	rotor disk speed
Φ	azimuthal coordinate

CHAPTER 1

INTRODUCTION

1.1 Background

Gas turbines are rotary engines that use air as the working fluid. These engines are widely used in aerospace, marine, oil & gas, and power industries for their high power-to-weight ratio and ease of maintenance.

These air-breathing engines usually employ the open Brayton cycle to extract power/thrust. In gas turbine engine, the ambient air is first adiabatically compressed in a multi-stage compressor to increase its pressure. This is then followed by an approximately isobaric combustion within a combustion chamber which increases the compressed air temperature. This high pressure, high temperature gas is then adiabatically expanded through a multi-stage turbine. The power required to run the compressor is extracted from the turbine. The excess energy of the gases is then used to provide either thrust or shaft power depending on the nature of application.

An important aim of the gas turbine designer is to increase its efficiency; this has both economic and environmental impacts. The efficiency of a gas turbine increases as the gas temperature at turbine entry, the turbine entry temperature (TET) is increased. Over the years the TET has increased from about 1000K to 1800K. So this temperature can be much higher than the melting temperature of turbine metal components. High TETs have been rendered possible by the advances made in materials, cooling, and sealing technologies.

A turbine stage contains a stationary part (stator) and a rotating part (rotor). The stator is provided with vanes which guide the main gas onto the rotor blades. A small portion of the high pressure, high temperature mainstream gas flowing across the vanes and the blades may be ingested into the space between the stator and the rotor (wheel space or disk cavity). Ingestion of hot main gas into disk cavity affects the highly stressed rotor disk's structural strength, thereby reducing its integrity and life.

The phenomenon of main gas ingestion into disk cavity has been a topic of research for the past four decades. Past studies have revealed that ingestion into the disk cavity is caused either by one or a combination of the following mechanisms, Johnson et al. (1994):

- disk pumping
- geometry in the rim seal region
- Asymmetries in the rim seal geometry
- periodic vane/blade pressure field
- turbulent transport in the platform/outer cavity region
- flow entrainment
- time-dependent flow structures within the cavity

Traditionally, the main gas ingestion has been controlled by installing seals on the rotor and stator rims and by pressurizing the disk cavities by the injection of secondary (or purge) air, which is bled from the compressor. Apart from cavity

sealing, the secondary air is also used for cooling of airfoil and cavity internals, bearing chamber sealing etc. As the secondary air does not get expanded in the turbine, there results a loss of efficiency. Nevertheless, this is a necessary loss as the presence of secondary air enables the engine to have higher TET. Figure 1.1 schematically depicts a typical gas turbine secondary air system.

The amount of main gas ingested into a disk cavity is influenced by the geometry of the rim seals and by the amount of secondary air provided to the cavity. Since the amount of secondary air used results in an efficiency loss, the gas turbine designer aims to minimize the secondary air amount.

The study of main gas ingestion and the sealing of turbine disk cavities by the means of rim seals and secondary air is the main topic of this thesis.

In this study, experiments were performed in a model single stage axial flow gas turbine. The turbine stage featured vanes, blades, rim seal on both rotor and stator and a labyrinth seal radially inboard of the cavity. Static pressure measurements in the cavity and in the main gas path and tracer gas concentration measurements in the cavity were carried out. The experimental results from this work are to be used to validate the predication of CFD simulations. Furthermore, the results will be used to develop an empirical correlation for main gas ingestion that can be incorporated in an internal secondary air system network model.

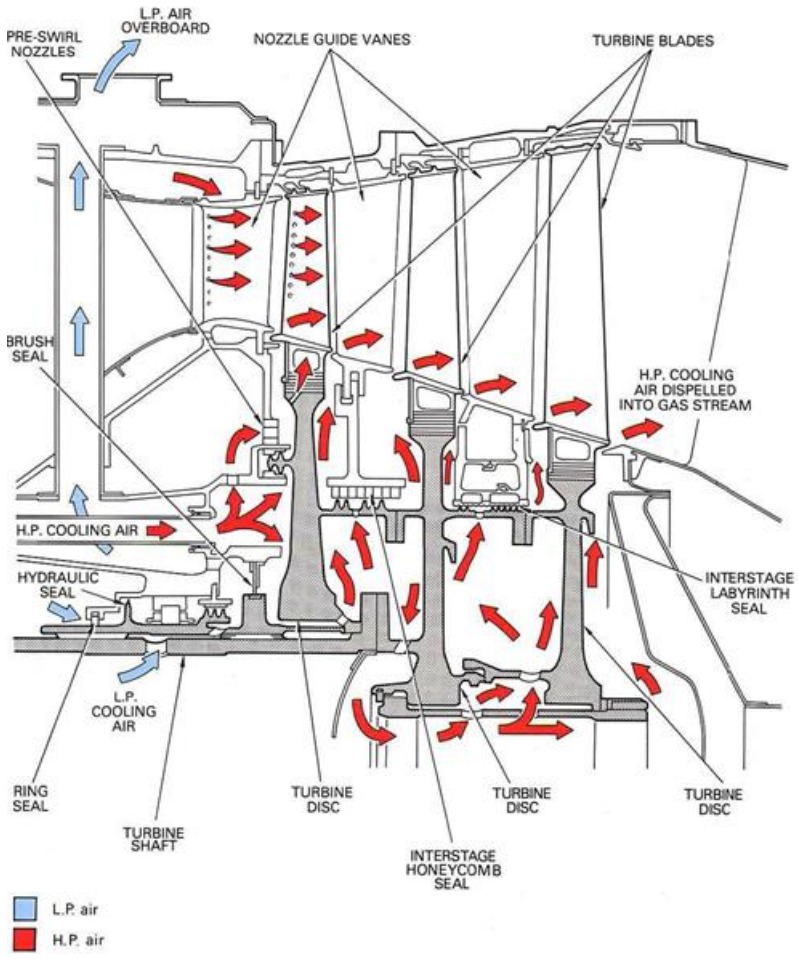

Fig 1.1 Schematic diagram - gas turbine internal secondary air system
(Courtesy: The Jet Engine, 1986)

1.2 Literature Survey

A large number of theoretical, computational and experimental studies have been performed to understand the main gas ingestion problem and the accompanying complex flow pattern in gas turbine rotor-stator cavities. Some of these that are relevant to the current work are briefly discussed below.

Abe et al. (1979) constructed a rig which featured vanes inboard of a mainstream annulus with no downstream blades. 27 vanes were positioned upstream of the rim seal clearance, they turned the main air flow by 50 degrees.

Several rim seal geometries were investigated including axial clearance and hook seals. The authors identified ingress as predominantly governed by the following: the ratio of the velocities of the sealing air and the flow in the annulus, the rim-seal clearance, and the rim seal geometry.

Phadke and Owen (1983) investigated a simple rotor-stator system with peripheral seal variation. One axial-gap and four radial-gap seal configurations were tested using a pressure criterion as the key ingestion indicator. A pressure inversion effect occurred for radial overlap seals where the cavity pressure increased with increasing rotational speed. This effect was attributed to the flow entrained near the rotor impinging on the stator face and forming a high-pressure region. It was also found that the radial overlapping seals required less sealing flow to prevent ingestion than that required for an axial-clearance seal. Thus the pressure inversion effect was seen to be beneficial.

Further tests were conducted by Phadke and Owen (1988a) with a rotor-stator rig in a quiescent environment (no external flow). Flow visualization, measurement of pressure and tracer gas concentration techniques was employed for different seal geometries to understand mainstream gas ingestion associated flow field. For all configurations, the sealing flow entered axially, impinged on the rotor and then flowed outward as a radial wall jet. The radial clearance seal was found to have the highest sealing effectiveness among the various rim seal geometries that were considered. For each of the rim seals, a theoretical correlation was proposed for the $C_{w,min}$ value. $C_{w,min}$ was found to depend on the

rim seal geometry as well as the rotational Reynolds number. Phadke and Owen extended their research to include the effect of the mainstream annulus air flow rate on ingestion (1988 b, c). It was found that ingestion occurred because of the circumferential asymmetry of the mainstream gas static pressure rather than the mainstream gas flow rate itself. It was shown that increasing the circumferential pressure asymmetry in the annulus flow at the rim seal increased the minimum sealing flow required and that for certain conditions, $C_{w.min}$ was independent of the rotational Reynolds number. This work has also been discussed in a comprehensive book on rotating disk flows by Owen and Rogers (1989).

Chew (1991) aimed to develop a theoretical model for ingestion, using available experimental data. The model worked by linking the boundary layer flow inside the wheel space to the rim seal, which was treated as an orifice. As the boundary-layer flow in a rotating-disk system depends on the turbulent flow parameter λ_T, Chew used this parameter in his model. It was hoped that the integral momentum equation solution for the flow between two discs would provide a basis from which to develop more elaborate models. His prediction agreed reasonably well with Phadke and Owen measurements of $C_{w.min}$. The author also deduced that in the absence of purge air flow, the amount of main gas ingestion was of the order 20 percent of C_{wmin} (for that particular seal).

Hamabe and Ishida (1992) studied ingestion caused by non-axisymmetric external flow. They suggested that whilst many previous researches had assessed the minimum sealant flow rate required to prevent ingestion, few had estimated

the ingestion flow rate itself, or considered the shape of the external flow pressure profile. A rotor-stator rig featuring vanes in the external annulus was used to generate non-axisymmetric flow. Concentration taps were used to produce sealing effectiveness plots, similar to previous works. 24 static pressure taps were used to measure the external flow pressure non-axisymmetry. It was found that the sealing effectiveness largely depended on the shape of the circumferential pressure distribution in the mainstream gas path.

Green and Turner (1994) were the first to perform experiments with a fully equipped rotor-stator system featuring guide vanes and rotor blades. Using a simple axial clearance seal configuration they compared four different external flow cases. It was shown that the no-external flow condition produced the least ingestion and the setup with only the vanes present (i.e. no blades) produced the most ingestion. The full stage case (i.e. vanes as well as blades) showed a reduction in the ingested flow. It was suggested that the rotor blades rendered the mainstream gas flow more axisymmetric and thus reduce ingestion.

Johnson et al. (1994) identified the physical mechanisms inherent in the ingestion process such as disk pumping, circumferential pressure asymmetry in the main gas path, periodic pressure fluctuation due to vane/blade interaction, and turbulent transport in the fluid. It was concluded that these mechanisms, among others, needed to be well understood before designing advanced industrial gas turbines.

Roy et al. (1999, 2000, 2005, 2007, 2011) carried out experiments in a model single-stage axial turbine stage with blades, vanes, and rim seals on the stator and rotor. Unsteady, as well as time-averaged, static pressure measurements were made at various locations in the disk cavity and main gas path. A tracer gas (CO_2) technique was employed to measure ingestion at several radial locations in the cavity. Particle image velocimetry was employed to map the flow within the disk cavity. These measurements helped better understand the nature of the main gas path and disk cavity flows.

Gentilhomme et al. (2002) reported experimental measurements in a single-stage axial turbine, steady and unsteady CFD simulations of the same, and an elementary model of ingestion. Distribution of time-average pressure and ingestion were measured. The results suggested that the vane trailing edge wake was a stronger driver for pressure asymmetry (which is the dominant ingestion driving mechanism) than the blade for the particular rim seal geometry.

Cao et al. (2003) reported a combined experimental and computational (CFD) study of the interaction between the mainstream gas flow and the sealing air flow. The experiments were performed in a two-stage axial turbine rig featuring a simple axial gap between the rotor and stator disks, without any rim seals. The first stage of the turbine is used to provide representative flow conditions into the second stage. The second stage has 50 fixed vanes and 67 rotating blades. A three-dimensional unsteady simulation of the flow (without the vanes and blades) was carried out. An unsteady flow structure in the outer region

of the disk cavity was predicted. Alternate regions of ingress and egress, which rotated at 90-97% of rotor speed, were found near the cavity rim.

Bohn et al. (2006) compared an axial and a radial seal configuration using a 1.5-stage axial turbine with blades and vanes. A comprehensive analysis of 115 pressure/concentration points was taken inside the rig using a Scanivalve setup. A strong effect of rim seal configuration was found on the sealing efficiency. The radial seal was shown to outperform the axial seal- i.e. less sealing flow was required to purge the wheel space.

Recently, Johnson et al. (2008) proposed a two-orifice model of ingestion incorporated two discharge coefficients: one for ingestion ($C_{d,i}$) and another for egress ($C_{d,e}$). Also considered was the addition of a radial momentum term to account for swirl effects in the seal mixing region. This work showed improved seal characterization compared to the earlier one-discharge coefficient models. Experimental ingestion results from Arizona State University (ASU) were well predicted by the two-orifice model with values of $C_{d,e} = 0.27$ and $C_{d,i} = 0.20$. The new model appears to better characterize rim seals of a wider range of configurations.

1.3 Overview of the present work

In this work, experiments were carried out in a model single-stage axial-flow air turbine with blades, vanes, rim seals on both the stator and rotor, and a labyrinth seal radially inboard in the disk cavity. Though simpler than an actual

gas turbine stage, the model stage retained the key features which influence the phenomenon of main gas ingestion.

The organization of this thesis is as follows: Chapter 2 contains a description of the experimental facility, the techniques and procedures for measuring the time-average static pressure in the main gas path and the disk cavity and ingestion in the disk cavity. Chapter 3 contains the experimental results and their discussion. Finally, Chapter 4 summarizes the conclusions and suggests some recommendations for future research.

CHAPTER 2

RESEARCH FACILITY AND EXPERIMENTS

2.1 The Experimental Facility

Figures 2.1 and 2.2 show the experimental facility that was used for the present work. The facility is an open air-flow system, where lab ambient air is drawn into the system and is discharged to the atmosphere.

Main air flow

The turbine mainstream air is supplied by a centrifugal blower (Hauck, 22.4 kW, TBA-20-30) can provide an air flow-rate of up to 1.42 m^3/s (≅ 3000 cfm) and is controlled by a variable-frequency motor drive (Cutlet Hammer, AF 95).The blower inlet is connected to a 292 mm (11.5") i.d. plexiglass circular duct via a diffuser with a divergence angle of 5 degrees. The blower discharges air to the atmosphere through a 2.235 m (7'4") long, 311 mm (12.25") diameter vertical pipe connected to an exhaust duct.

Measurement of mainstream air flow rate

The main air flow rate is measure by a pitot tube rake. The rake is equipped with five pitot-static tubes equally spaced along a manifold and is installed in the 292 mm (11.5") i.d. plexiglass exit duct at approximately 950mm (37.4") upstream of the main blower inlet. The pitot tube rake is connected to a digital manometer (Validyne, PS309, range: 0-2" water gauge) which provides an analog output (0-2V) of the air flow dynamic pressure. The output is routed to a

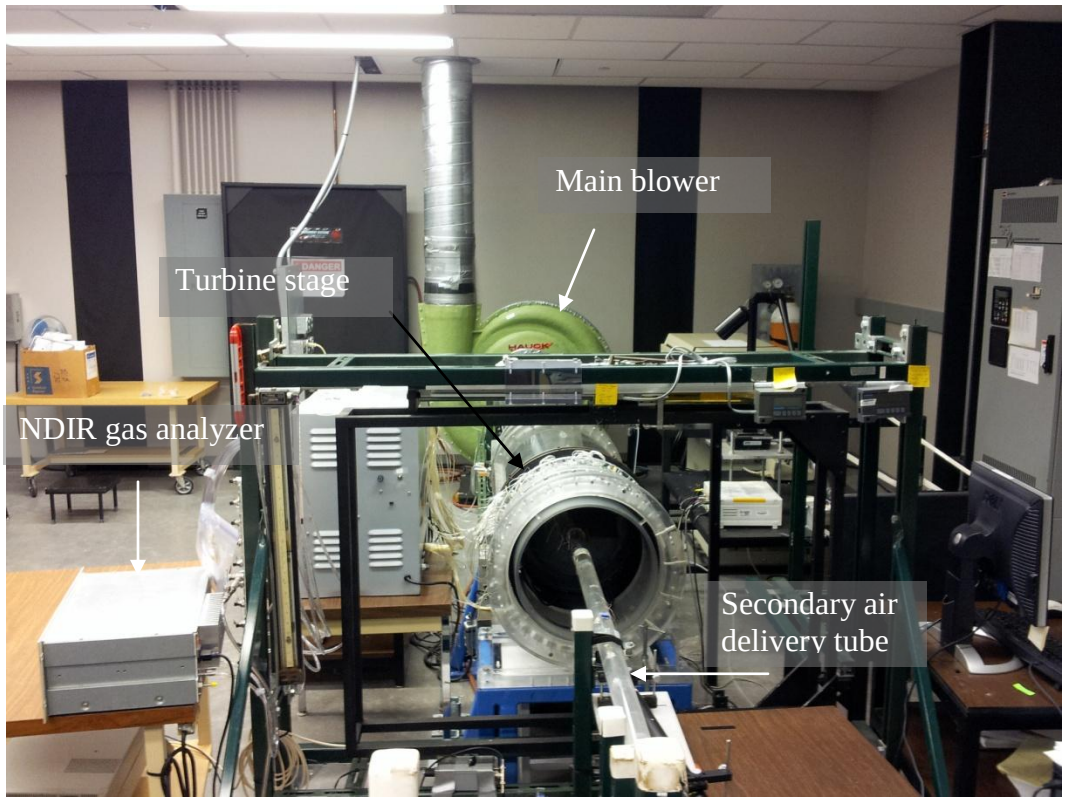

Fig 2.1 Axial Flow Turbine experimental facility.

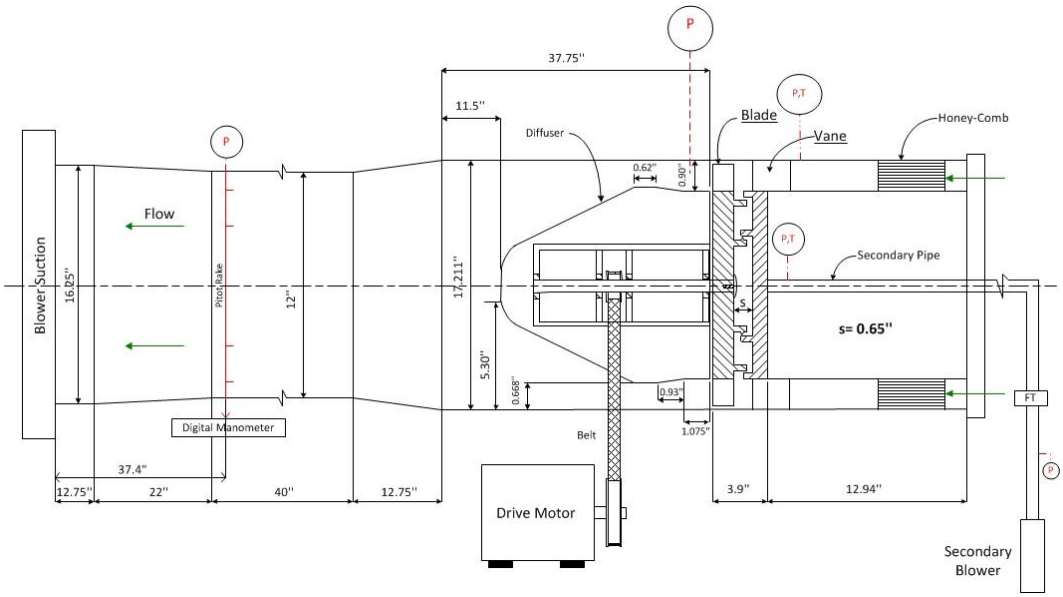

Fig 2.2 Schematic of ASU Turbine rig.

data acquisition system (Analogic, DATA 6500) where the mean and RMS values of the dynamic pressure are calculated and displayed.

Secondary (or purge) air flow

The secondary air is supplied by a smaller centrifugal blower (2.24kW, Hauck, TBA-16-3) also controlled by a variable-frequency motor drive (Emerson, Prism). The maximum flow rate that can be provided by the blower is 0.12 m^3/s (≅ 250 cfm). The blower discharges air into a 50.8 mm (2.0") nominal diameter insulated galvanized iron pipe to a turbine flow meter. The air then flows through a check valve to a 1.780 m long, 38.1 mm i.d plexiglass pipe to the centre (hub) of the disk cavity. To straighten the air flow, a honeycomb section (12.7 mm (0.5") long, 3.2 mm (0.126") hexagonal cell size) has been installed in the plexiglass pipe 1.60 m (63.0") upstream of the cavity inlet.

Measurement of secondary (purge) air flow rate

The turbine flowmeter mentioned earlier (EG&G Flow Technology, FT-32) measures the secondary air volumetric flow rate. The flow meter indicator provides an analog output signal that is routed to a digital multimeter (Model 45, Fluke). Based on a known calibration, this voltage is then converted to air volumetric flow rate.

Test section

The rotor-stator turbine stage section is located on the suction side of the main air blower. This allows optical access to the test section in both axial and

radial directions. The rotor is driven by a motor in addition to the rotation imparted by the main air flow.

Rotor drive

The rotor disk was mounted on a 50.8 mm (2.0") mild-steel shaft. The shaft is belt-driven by a 2.24 kW (3HP, 1750 rpm max, GE) motor whose speed is controlled via a 3.73kW adjustable-frequency drive (5 HP, Eaton-Cutler Hammer). The speed ratio of the rotor disk to the motor wheel is 3.27:1; this allows a maximum rotor speed of 5720 rpm. The rotor speed is measured by a digital photoelectric tachometer (Biddle Instruments; accuracy ±1 rpm). The AFD helps maintain the speed of the rotor constant. The AFD is also equipped with a dynamic braking resistor (Power-Ohm Resistors, P13549-405, rated at 2.8 kW at a total resistance of 65.0Ω) which enables a quick shut-down of the motor.

2.1.1 The Turbine Stage

Figure 2.3 shows the schematic of the turbine stage which was used in the present study. A 120.7 mm (4.75") long honeycomb section (Polypropylene, 0.315" cell size, black, Plascore, PP30-5) has been provided in the annular main air passage 152.4 mm (6.0") upstream of the vanes to straighten the incoming flow.

The plexiglass stator is 19.1 mm (0.75") thick and has a diameter of 391.4 mm (15.4"). There are 22 partial-height, full length vanes which turn the incoming air by 68.6^0, thereby imparting a realistic swirl to the air flow. The aluminum rotor disk is of the same diameter as the stator with 28 partial-length

and partial-height blades. The blade tip clearance (with the steel outer shroud) is 1.5 mm (0.059”). The blade and vane heights are such that given the main blower capacity, sufficiently high main air stream-wise velocity can be obtained so as to result in an acceptable velocity triangle upstream of the blade row at prescribed rotor speeds. The axial gap between the rotor and the stator (identified as disk cavity) is maintained constant at 16.5 mm (0.65”). The purge gas is injected into the inner cavity at the stator hub by a 1780 mm (70.1”) long, 38.1 mm (1.5”) i.d. plexiglass tube.

Rims seals are provided on the rotor and stator disks. The rim seals have an axial overlap of 2.6 mm (0.102”) and a radial gap of the same magnitude. The disk cavity also features a labyrinth seal radially inboard that has a radial clearance of 0.51 mm $\pm$ 0.01 mm. This effectively divides the disk cavity into an ‘*Inner Cavity*’ and a ‘*Rim Cavity*’, (figure 2.3).

The mid-span shapes of the vanes and blades are also shown in figure 2.4(a). Figure 2.4 (b) shows the velocity triangle diagram for the mainstream gas at the vane exit and the blade exit. β_2 is the angle, with respect to the axial direction, of the mainstream gas velocity (W_2) relative to the blade. A positive value of β_2 ensures that the rotor operates as a turbine. Appropriate combination of rotor speed and main gas flow rate ensures an adequately a large positive value of β_2.

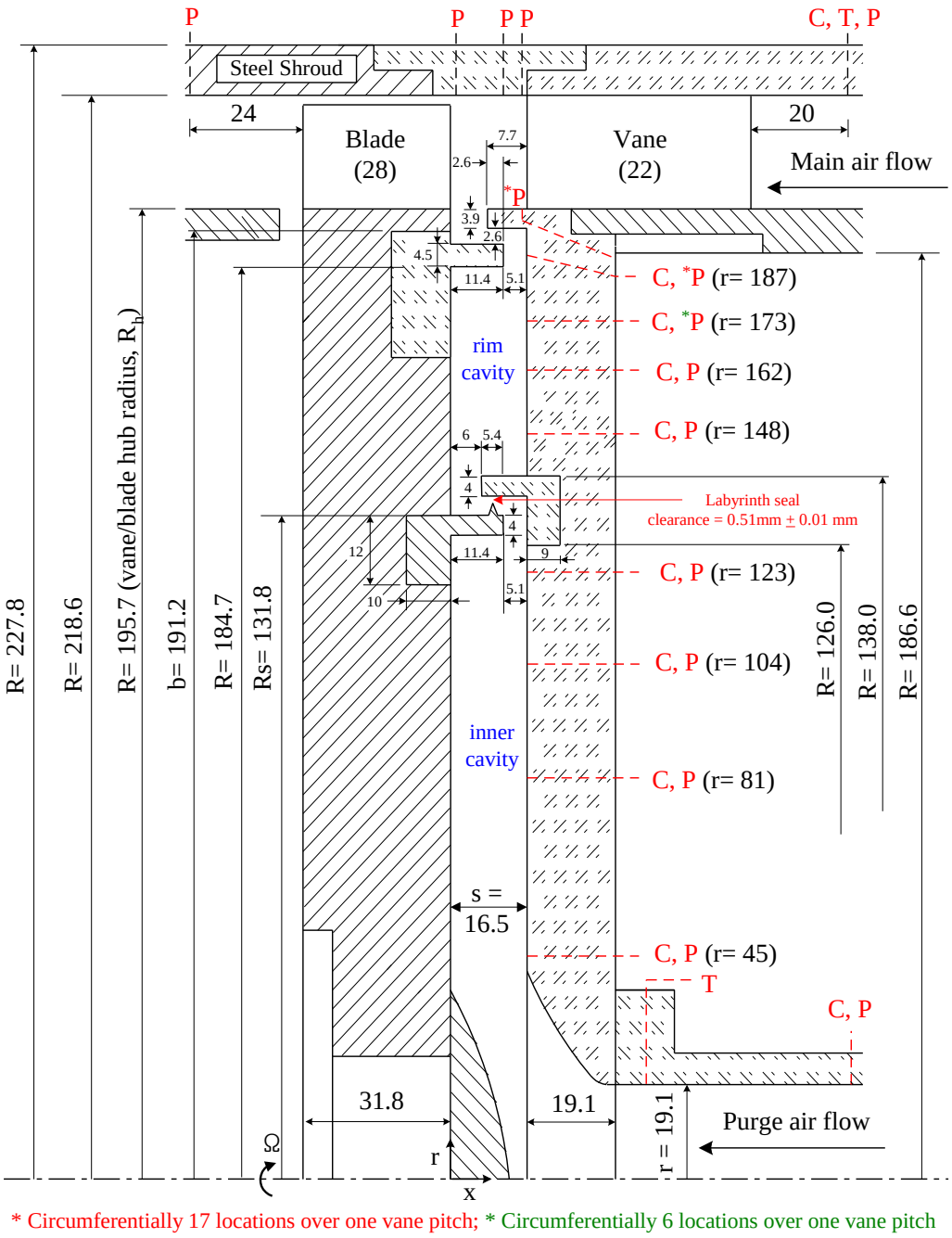

* Circumferentially 17 locations over one vane pitch; * Circumferentially 6 locations over one vane pitch

Fig 2.3 Schematic diagram of the single-stage rim-seal arrangement (C: Gas concentration tap, P: time-average static pressure tap, T: thermocouple); all dimensions are in mm.

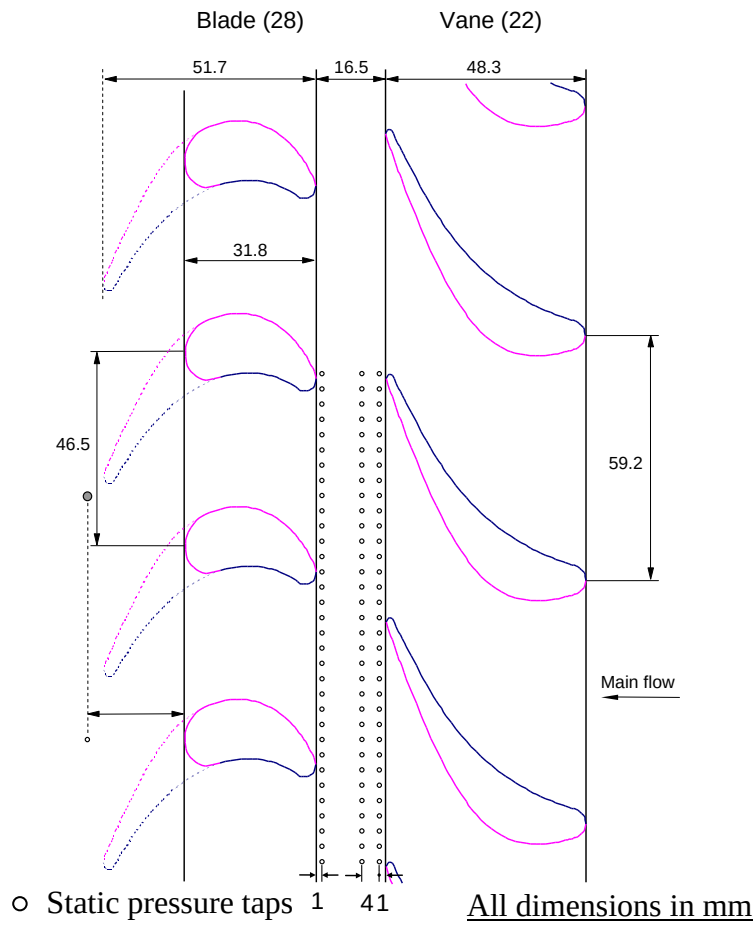

(a) static pressure taps on outer shroud

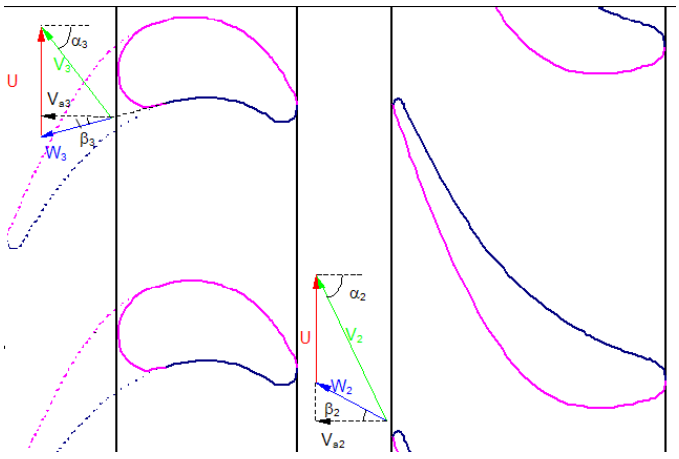

(b) Main air velocity triangle

Fig 2.4 The blade and vane arrangement.

2.2 Time-Average Static Pressure Measurement

2.2.1 System Components

A differential pressure transducer (DPT), a Scanivalve and a signal carrier demodulator were used to measure the time-mean static pressure distributions. The measurements were made at the stator disk and in the main gas path at the vane platform and at the outer shroud. Figure 2.5 displays the components which are described briefly in the following section.

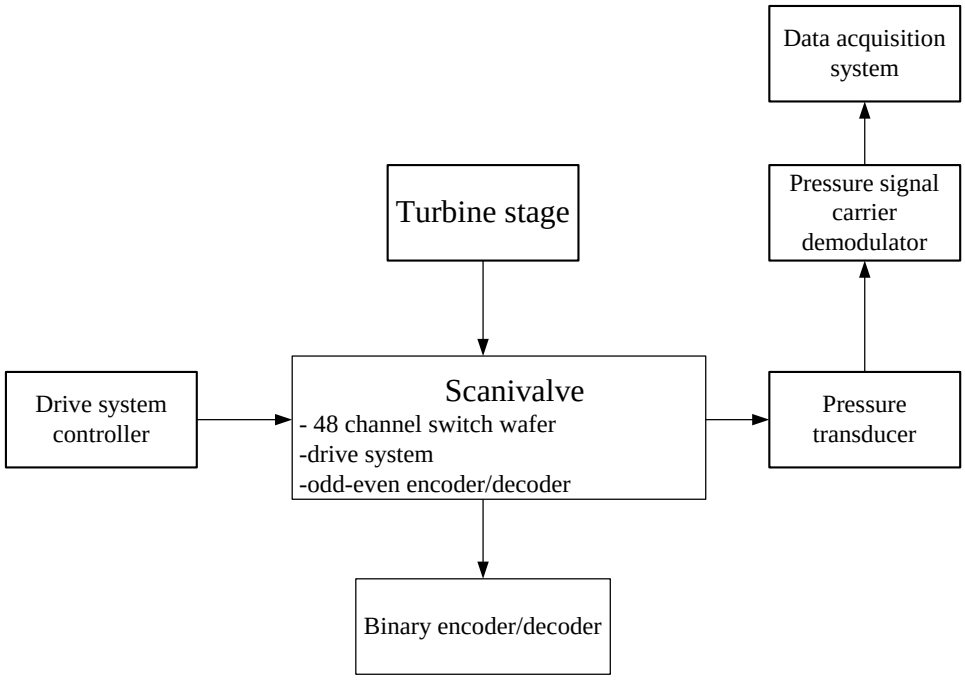

Fig 2.5 Pressure measurement system

Scanivalve

The Scanivalve is a pressure sampling scanner for measuring multiple pressures. It enables a pressure transducer and the associated zeroing circuit to do the work of 48 transducers and 48 zeroing circuits albeit sequentially. The unit employed in the current work has three main subcomponents: samplivalve, binary encoder/decoder and drive system controller.

A solenoid-controlled stepper drive rotates the 48-channel fluid switch wafer such that, at any particular time, only one inlet port is connected to the outlet port. A position encoder/decoder transmits the angular position of the Scanivalve to a display system from which information regarding particular channel connected to the outlet could be read off.

Pressure Transducer

A variable reluctance-type pressure transducer (DP-45, Validyne) with a range of 0-2 psi was used. The transducer contains two ports, one of which is connected to the Scanivalve outlet and the other is open to ambient air. Thus, the transducer measures gage pressure. The transducer contains a sensing diaphragm which produces an output voltage corresponding to the applied pressure differential.

Carrier Demodulator

The pressure signal carrier Demodulator (Validyne CD 12) features a high pass filter and suppression mode. It converts the pressure transducer outlet into a DC voltage signal. This signal can be routed to a data acquisition system. It has a

high input sensitivity range (0.9 to 75 mV/V); this allows tracking of even small fluctuations in the input signal. There is also a digital display which gives the pressure in terms of voltage (0-10V).

Data Acquisition System

The analog signal from the pressure signal carrier demodulator is routed to the data acquisition system via a BNC cable. The data acquisition system used in the present work is a Universal Waveform Analyzer (Analogic, DATA 6500). It was programmed to provide the time-mean and RMS of the static pressure signal over sequences of 30720 data points with sampling period of 500μs (2 kHz sampling frequency).

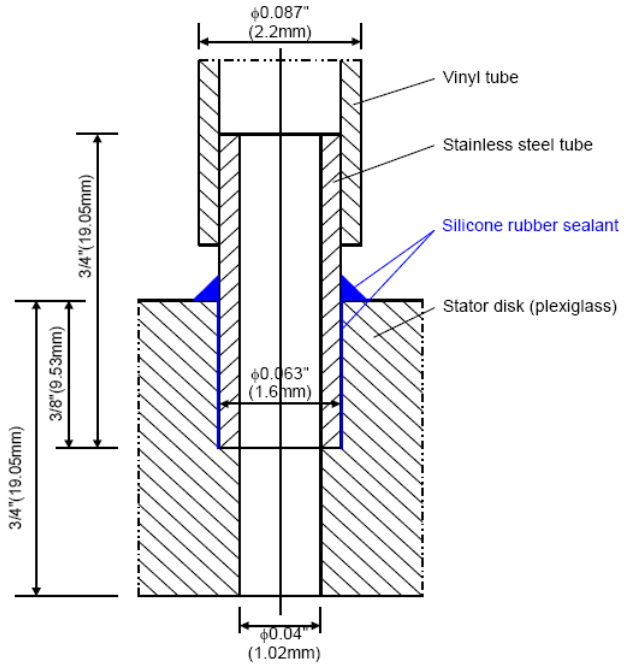

Fig 2.6 Schematic of static pressure tap on stator disk

2.2.2 Experimental Procedure

As mentioned earlier a total of 48 pressure channels are available in the Scanivalve system. Figure 2.6 shows a schematic of a pressure tap used in the experiments. It is ensured that no machining burrs are present near the pressure tap as they could affect flow condition. Static pressure measurements have been conducted at the following locations:

a) For the static pressure distribution in the main gas path, 33 pressure taps, distributed over two vane pitches are provided on the outer shroud at 1mm, 5 mm and 15.5 mm downstream of the vane trailing edge;

b) For the radial distribution of static pressure at the stator surface, eight pressure taps at r=45mm, 81mm, 104mm, 123mm, 148mm, 162mm, 173mm, 187mm are provided along a radial line;

c) At the stator surface, 17 pressure taps at r = 187 mm and 6 pressure taps at r = 173 mm are provided circumferentially over one vane pitch for measuring the circumferential distribution of pressure;

d) For the static pressure distribution on the vane platform, 17 pressure taps are provided circumferentially over one vane pitch at 1mm downstream of vane trailing edge.

The main air inlet gage pressure is measured using a pressure tap at the outer shroud 20 mm upstream of the vane leading edge plane. The secondary air

inlet gage pressure is measured at a tap located 70 mm upstream of the disk cavity entrance.

The time-average of the measured pressure is defined as

$$\bar{p} = \frac{1}{T}\int_0^T p(t)dt \approx \frac{1}{N}\sum_{i=1}^{N} p_i \qquad (2.1)$$

The data acquisition system was set to acquire 30720 points (N) at 2 kHz sampling frequency (500 μs sampling interval) to ensure that the fluctuations in the pressure readings are averaged out. The uncertainty in the time-average static gage pressure measurements was estimated to be ± 4%.

2.3 Mainstream Gas Ingestion Measurement

For these measurements, the purge air is seeded by a tracer gas (CO_2) before it is introduced into the disk cavity. The penetration of mainstream gas into the cavity is determined by measuring the CO_2 gas concentration in the cavity gas. Note that any ingestion of main gas (air) into the cavity reduces the concentration of CO_2 in the cavity gas. The cavity gas is sampled at multiple radial locations and the CO_2 concentration is measured using a gas analyzer (see Section 2.3.1). One can then calculate the efficacy of the rim seal and the purge air in sealing the cavity in the form of a 'sealing effectiveness'.

2.3.1 System components

NDIR gas analyser

An NDIR gas analyzer (Siemens- Ultramat 23) is used to measure CO_2 concentration. Its main components are: an infrared source, a sample chamber or light tube, and a wavelength sample chamber. The gas concentration is measured

electro-optically by its absorption of a specific wavelength in the infrared (IR). The IR light is directed through the sample chamber towards the detector. In parallel, there is a second chamber with a reference gas (typically nitrogen). The detector has an optical filter in front that eliminates all light except the wavelength that the molecules of the selected gas can absorb. At the back of the device, two inlets one for the sample gas, the other for the zero gas (N_2), and one gas outlet are provided. The permissible ranges for the sample gas pressure, flow, and temperature are, respectively, 0.5 to 1.5 bar absolute, 1.1 to 2 l/min, and 0 to 50° C. When switched on, the analyzer carries out a calibration (AUTOCAL) with the zero-gas (N_2). It calibrates the zero and sensitivity of the IR channel. The AUTOCAL can be manually triggered during operation by pressing the CAL key in the keypad.

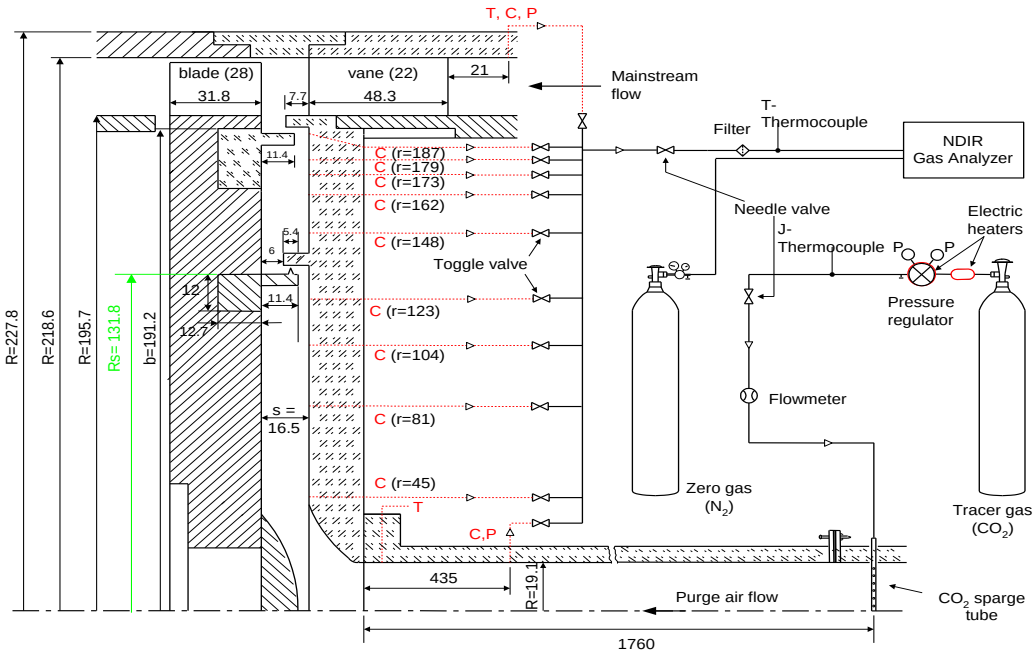

Fig 2.7 Arrangement for mainstream gas ingestion measurement for the single-stage turbine configuration.

Gas Cylinders and Tube Connections

The set-up and tube connections are shown in figure 2.7. Ultra high purity (99.9% N_2) compressed nitrogen gas was used as the zero-gas for AUTOCAL. The purge gas was seeded with CO_2 approximately 1.7m upstream of the disk cavity entrance using a sparger tube (stainless steel, 6.3 mm o.d; 4.5 mm i.d) containing 15 holes (each of 1 mm diameter). The volumetric concentration of the CO_2 was maintained at a fixed value (1 l/min) by controlling the CO_2 flow rate at the point of seeding, using a pressure regulator (on the gas cylinder) and a needle valve. To regulate the gas as it flows from the cylinder, an electric gas heater between the gas cylinder and the regulator, and a band heater at the back of the regulator is used. The heaters also help maintain the temperature of the tracer gas (measured upstream of the valve using a J-thermocouple) close to the desired temperature.

Each gas sampling tap was connected to a toggle valve by a vinyl tube (3/16" ID; 5/16" OD). The toggle valves were connected to a manifold with a single outlet. A needle valve and a filter were connected to the manifold outlet; a vinyl tube delivered the sample gas from the outlet to the gas analyzer.

2.3.2 Experimental Procedure

To measure ingestion in the cavity, the purge airflow is seeded with carbon dioxide (tracer) gas. The CO_2 volumetric concentration was measured just upstream of the entrance to the inner cavity and carefully maintained at 4.00 ($\pm$0.11) percent. The pressure taps at the eight radial locations on the stator disk

(figure 2.3) also serve as taps for measuring CO_2 concentration in the disk cavity. Stainless steel sampling tubes (1 mm i.d., 1.6 mm o.d.) are installed at radius r= 179 mm, 148mm, 104mm and were traversed axially, one at a time to measure the CO_2 concentration distribution in the disk cavity. The CO_2 concentration in the mainstream air is measured throughout the experiment to serve as a reference. The uncertainty in the measured CO_2 volumetric concentration is $\pm$ 0.11 percent CO_2 concentration. Due to the nature of the measurements, the measured ingestion is a time-averaged value over many rotor revolutions, but is local with respect to the circumferential vane position and the radial location in the cavity.

CHAPTER 3

RESULTS AND DISCUSSION

3.1 Experimental Conditions

The non-dimensional parameters in the experiments are: main air flow Reynolds number (Re_{vax}), rotational Reynolds number (Re_{φ}), and mass flow rate of purge air (c_w). These are given in Table 3.1. Time-averaged static pressure measurements were carried out in the main gas path to ensure steady and circumferentially periodic main air flow.

Table 3.1 Experimental Conditions

Exp. Set No.	Main air flow rate (cfm / Re_{vax})	Rotor Speed (rpm / Re_{φ})	Purge air flow rate (cfm / c_w)	β_2 (^{o})	Sec. flow rate/ Main flow rate (%)	Free Disk pumping flow rate (cfm / $c_{w,fd}$)
I	**2300** / 1.12×10^5	**2400** / 6.14×10^5	5 / 770	48.3	0.2174	57.3 / 9354
			10 / 1540		0.4348	
			20 / 3080		0.8696	
			30 / 4621		1.3043	
			40 / 6161		1.7391	
II	**1900** / 9.27×10^4	**1900** / 4.85×10^5	5 / 770	49.7	0.2632	47.4 / 7745
			10 / 1540		0.5263	
			20 / 3080		1.0526	
			30 / 4621		1.5789	
			40 / 6161		2.1053	

The rotor speeds and main air flow rates were chosen such that β_2 was large and positive, which ensured that the rotor operated in the turbine mode. The purge gas flow rates were chosen with reference to the free-disk pumping flow rate, this being the pumping flow rate due to the flat rotor disk rotating freely in a quiescent environment. Time-averaged static pressure and ingestion

measurements at the stator surface were performed for all of the experimental conditions at eight radial locations at r=45mm, 81mm, 104mm, 123mm, 148mm, 162mm, 173mm and 187mm. Time-averaged ingestion measurements in the disk (rim, inner) cavity at radial locations (r= 179 mm, 148mm, 104mm) were performed with a traversing probe for experiment set I and set II for all purge air flow rates except c_w=4621 and c_w=6161 .

Table 3.2 lists the values of the measured boundary conditions for the experiments. The static pressure of mainstream air at vane inlet and of purge air at inner cavity inlet changed slightly as the main air and purge air flow rates were changed.

Table 3.2 Measured boundary conditions

Static Pressure	Value
Average lab ambient pressure	101.3 kPa (absolute)
Average lab ambient temperature	23° C
Average pressure of mainstream air at vane inlet	99.8 kPa (absolute)
Average static pressure of purge air at disk cavity entrance	97.7 kPa (absolute)

3.2 Time-Average Static Pressure Distribution

Distribution of time-average static pressure in the main gas path were obtained over two vane pitches at three axial positions on the outer shroud and at one axial location on the stator rim seal (or platform). Also, the static pressure in the disk cavity at the stator surface was obtained at eight radial positions.

In figure 3.1, the circumferential distribution of pressure at the main gas path outer shroud and stator rim seal (platform) is shown for the experimental

condition Re_{vax} = 1.12×10^5, Re_φ = 6.14×10^5, c_w = 1540. The circumferential pressure variation produced by the vanes, and the decay of its strength axially downstream can be observed. The peak-to-peak amplitude is maximum at the outer shroud axial position immediately downstream from the vane trailing edge plane.

The pressure at the vane platform, 1mm downstream of the vane trailing edge plane, is considerably lower than the pressure at the outer shroud at the same axial position. On the other hand there is no discernible circumferential pressure variation at the stator disk even near its rim (r/R_h = 0.956) indicating that the pressure asymmetry in the mainstream flow is dissipated across the rim seals.

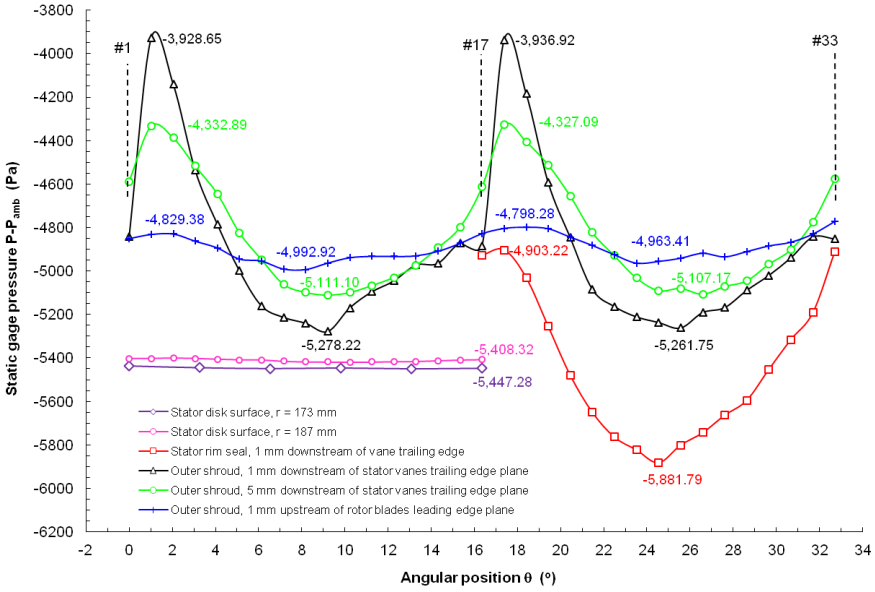

Fig 3.1 Circumferential distributions of time-average static gage pressure at the outer shroud, vane platform and stator near its rim – Re_{vax}= 1.12×10^5, Re_φ= 6.14×10^5, c_w = 1540.

The influence of purge air flow rate on the circumferential distribution of time- average static pressure is shown in figures 3.2 and 3.3 for experimental sets I and II, respectively. Although the effect of purge air flow rate (c_w) increase on the pressure distribution is not significant, the pressure level reduces slightly as the purge air flow rate increases. This could be due to the entry of lower pressure purge air from rim cavity into the main gas path, which in turn reduces the pressure difference between the main gas path and the rim cavity thereby reducing the potential for main air ingestion. It can also be observed that the pressure level in the main gas path is lower for set I in comparison to set II (by about 1.1 to 1.2 kPa). This may be due to the higher suction induced by the main blower (to deliver higher main air flow rate), this inducing lower pressure in the main gas path.

Figures 3.4 and 3.5 show the radial distributions of time-average static pressure at the stator surface in the disk cavity for set I and II conditions. As c_w increases, the pressure level in the 'inner cavity' rises due to the flow restriction posed by the labyrinth seal. This flow restriction results in a significant pressure drop across the seal to such an extent that the pressure distribution in the 'rim cavity' for different c_w's becomes essentially equal as shown in Figures 3.4 and 3.5. This phenomenon may be undesirable, because the primary intent of increasing c_w is to pressurize the rim cavity to minimize main gas ingestion. This pressurization of the rim cavity is not achieved in this configuration. Also to be

noted is that even though the static pressure within the rim cavity is similar for different c_w's, its value is somewhat spread out near the rotor rim seal.

The pressure distribution in the main gas path in conjunction with that in the rim cavity may help identify locations of ingress and egress. It may be suggested that the pressure at the downstream edge of the vane platform (stator rim seal) influences ingestion.

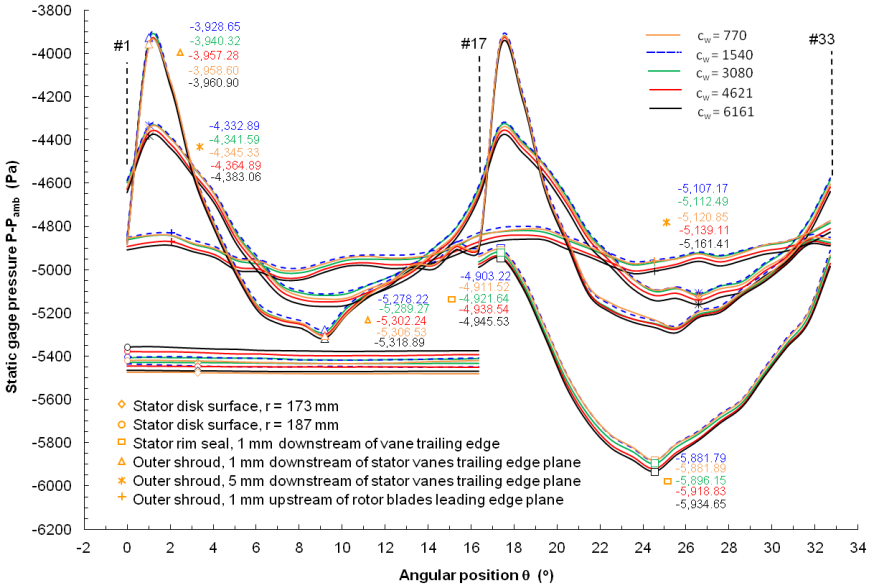

Fig 3.2 Effect of c_w on the circumferential distributions of time-average static pressure at the outer shroud, vane platform and stator near its rim- $Re_{vax}= 1.12\times10^5$, $Re_\varphi= 6.14\times10^5$ (experimental set I).

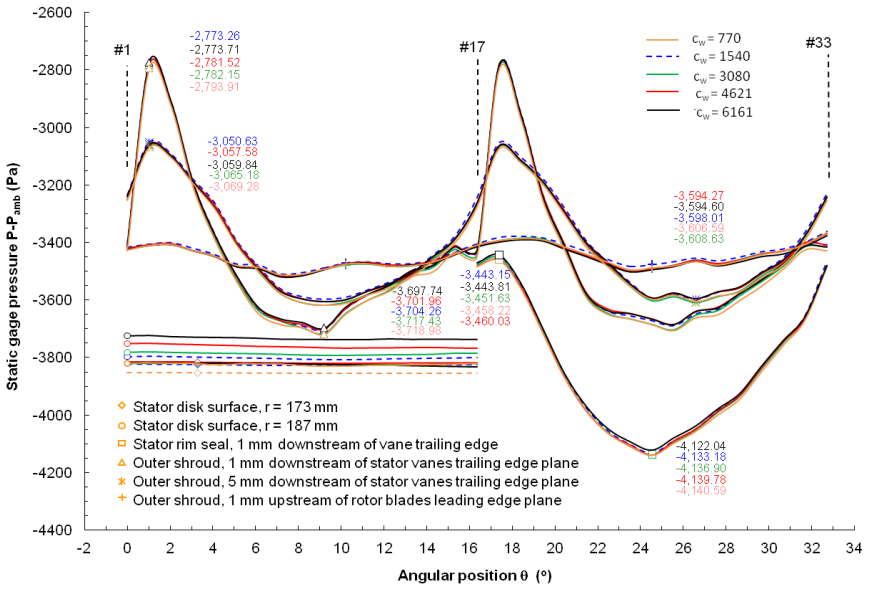

Fig 3.3 Effect of c_w on the circumferential distributions of time-average static pressure at the outer shroud, vane platform and stator near its rim- $Re_{vax}= 9.27\times10^4$, $Re_\varphi= 4.85\times10^5$ (experimental set II).

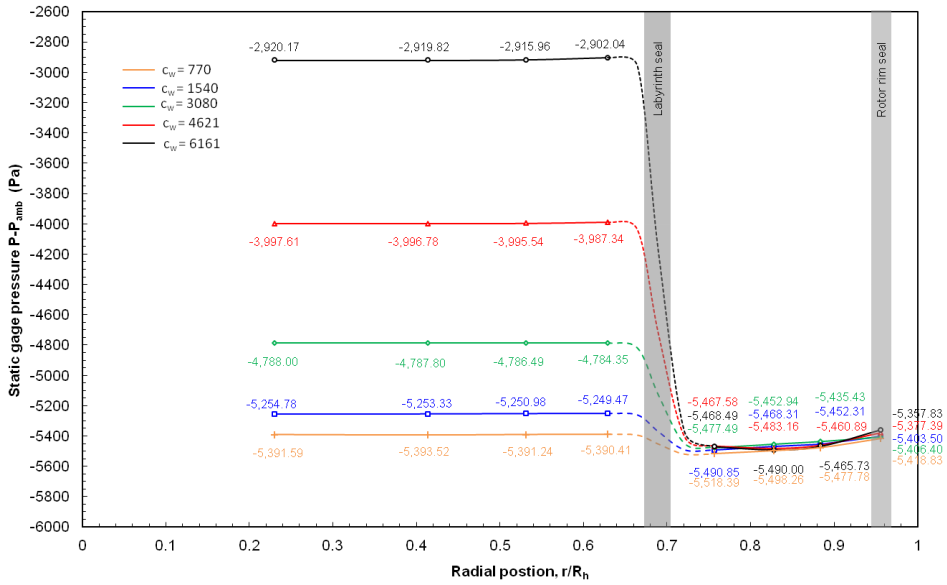

Fig 3.4 Effect of c_w on the radial distributions of time-average static pressure in the disk cavity at the stator surface- $Re_{vax}= 1.12\times10^5$, $Re_\varphi= 6.14\times10^5$ (experimental set I).

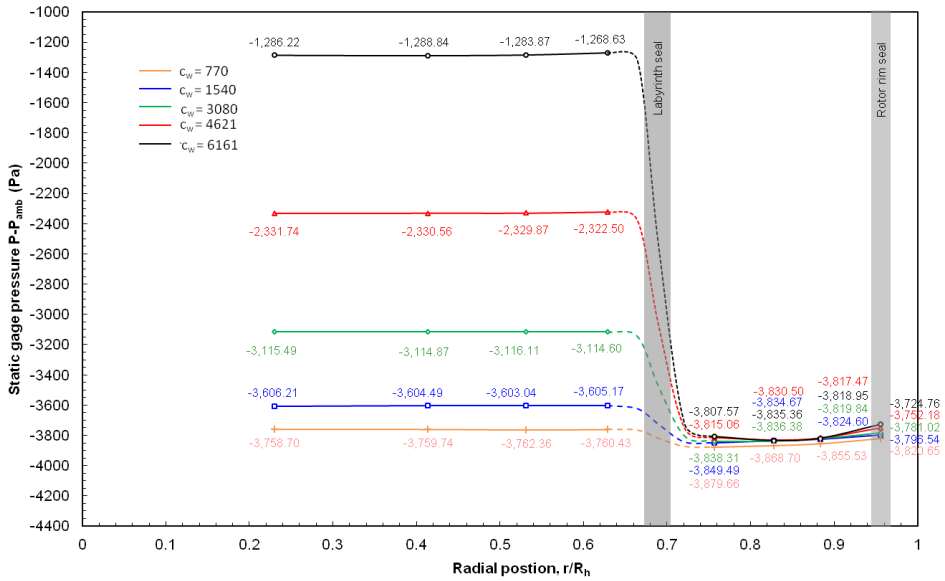

Fig 3.5 Effect of c_w on the radial distributions of time-average static pressure in the disk cavity at the stator surface- Re_{vax}= 9.27×10^4, Re_φ= 4.85×10^5 (experimental set II).

For this purpose the static pressure at the downstream edge of the vane platform (which is 7.7mm downstream of the vane trailing edge plane) was estimated from the pressure measurements. It must be kept in mind however, that the pressure in both the main gas path and the rim cavity is unsteady and that it is the instantaneous pressure field, which contains an unsteady blade-periodic component which is key to ingestion.

Figures 3.6 through 3.10 show the estimated circumferential pressure variation at the downstream edge of the vane platform for experimental set I. As mentioned earlier, the difference in the pressure between the main stream gas path and the disk cavity near its rim governs ingestion. In the figures, the estimated pressure at the vane-platform edge is compared to the measured pressure at r=187mm of the

stator surface. The 'red' and 'blue' areas depict the possible circumferential locations of 'ingestion' and 'egress' respectively in the 2 vane pitch sector, at least on the basis of time-averaged pressures. It should be noted that the circumferential extent of the 'ingestion' region decreases as c_w increases. The inference is that as c_w increases there is less ingestion of main gas into the rim cavity.

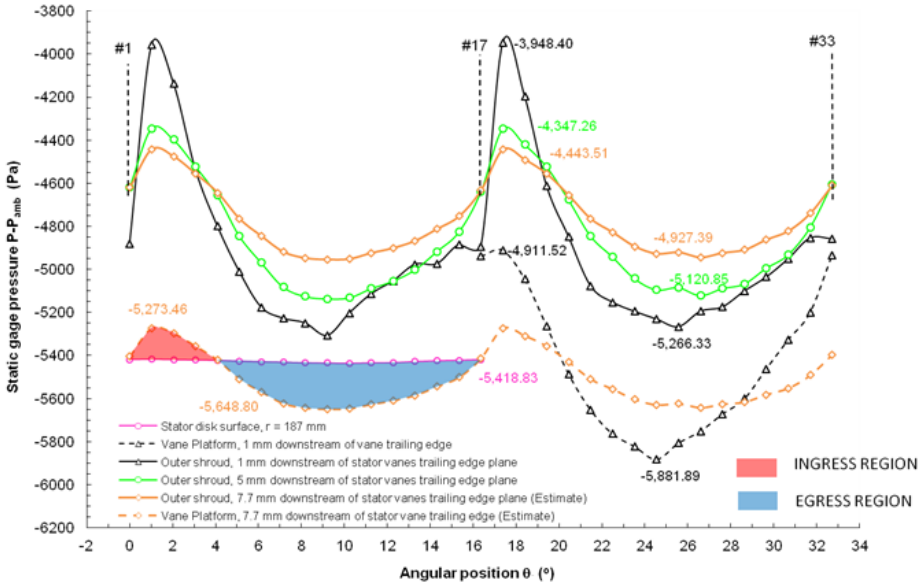

Fig 3.6 Circumferential distributions of time-average static pressure at the outer shroud, vane platform and stator surface near its rim – Re_{vax}= 1.12×10^5, Re_φ= 6.14×10^5, c_w = 770.

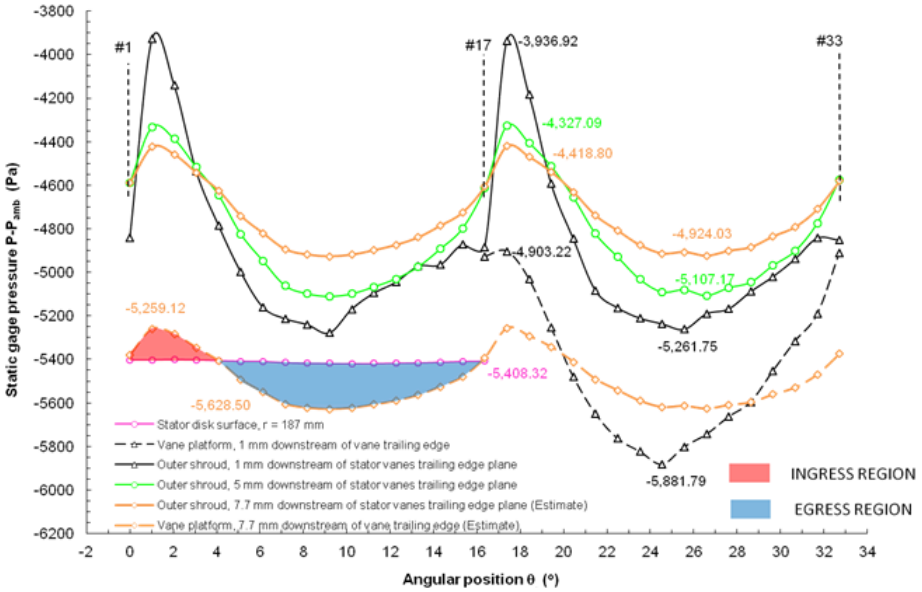

Fig 3.7 Circumferential distributions of time-average static pressure at the outer shroud, vane platform and stator surface near its rim – Re_{vax}= 1.12×10^5, Re_φ= 6.14×10^5, c_w = 1540.

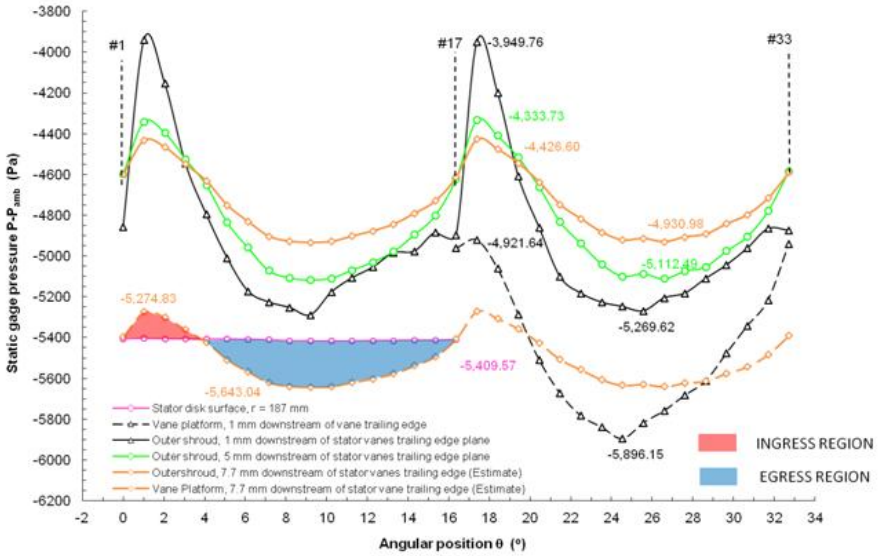

Fig 3.8 Circumferential distributions of time-average static pressure at the outer shroud, vane platform and stator surface near its rim – Re_{vax}= 1.12×10^5, Re_φ= 6.14×10^5, c_w = 3080.

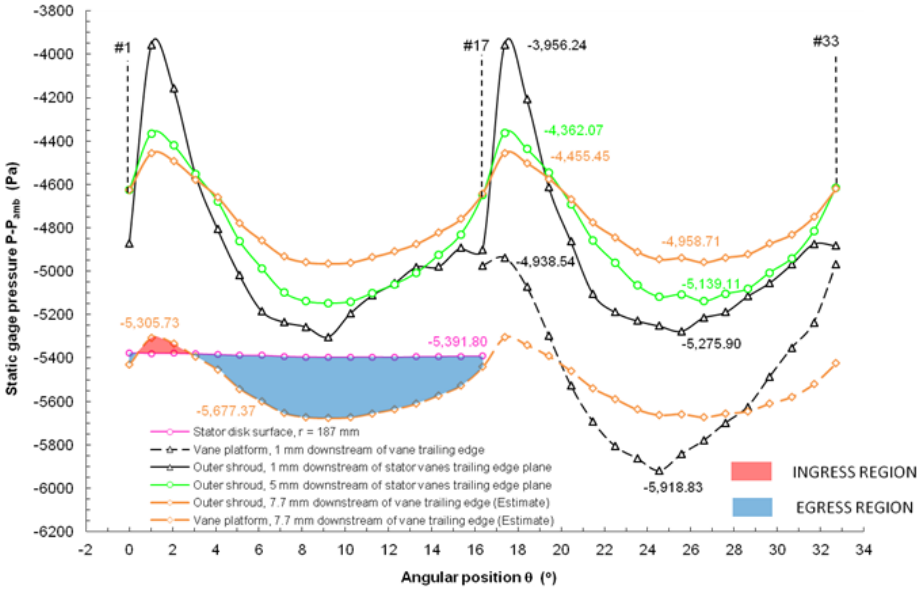

Fig 3.9 Circumferential distributions of time-average static pressure at the outer shroud, vane platform and stator surface near its rim – Re_{vax}= 1.12×10^5, Re_{φ}= 6.14×10^5, c_w = 4621.

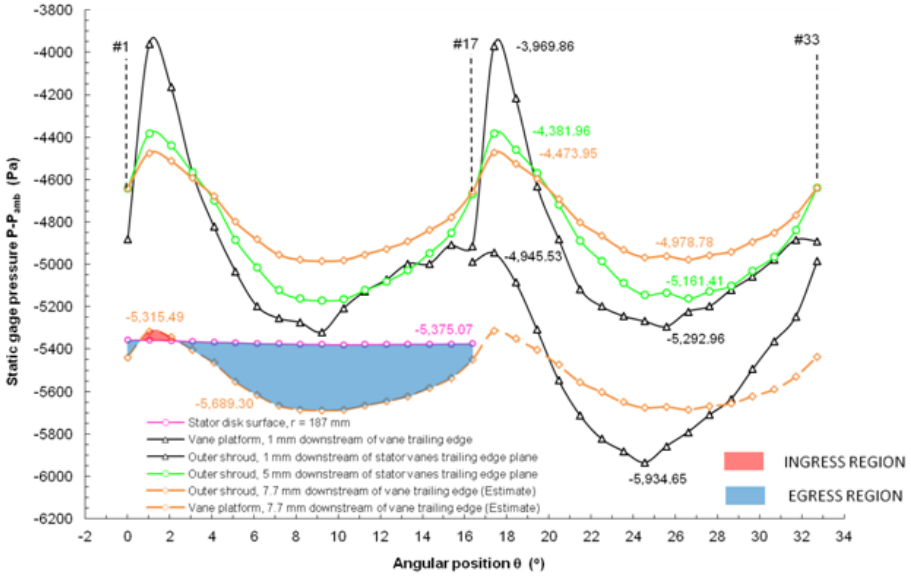

Fig 3.10 Circumferential distributions of time-average static pressure at the outer shroud, vane platform and stator surface near its rim – Re_{vax}= 1.12×10^5, Re_{φ}= 6.14×10^5, c_w = 6161.

3.3 Mainstream gas ingestion

All ingestion distributions are presented in terms of sealing effectiveness. Sealing effectiveness represents the combined effects of the rim seals and the purge air flow in countering ingestion. It is defined as

$$\eta(\underline{r}) = \frac{C(\underline{r}) - C_{main}}{C_{purge} - C_{main}} \qquad (1)$$

In the above expression, C represents the mass concentration of the tracer gas CO_2 in the cavity fluid. The value of η ranges from 0 (no sealing) to 1.0 (perfect sealing).

3.3.1 Measurements on the Stator Surface

Figures 3.11 and 3.12 show, respectively, the radial distributions of sealing effectiveness for experimental sets I and II. It can be seen that increasing the rotor speed and the main gas flow rate (set I) at a particular c_w decreases the sealing effectiveness. This can be explained as the combined effect of higher disk pumping at higher rotor speed and the higher pressure differential at main gas flow rate between the main gas path and the rim cavity. Both of these effects influence main gas ingestion. It can be remarked that for both set I and II conditions, as the c_w increases the sealing effectiveness increases concomitantly in the rim cavity region. The sealing effectiveness of the inner cavity decreases however for increasing purge air flow rates; this is consistent for set I and II conditions. It is remarked that this trend was repeatable experimentally. An explanation for the decrease in sealing effectiveness in the inner cavity could be

the possible presence of unsteady low-pressure structures -similar to those found by Cao et al. (2003) and Jakoby et al. (2004) in the rim-cavity- in the inner cavity. This may cause ingestion of rim cavity gas into the inner cavity. Further explanation is provided in section 3.4.

3.3.2 Axial Traverse Measurement in the Disk Cavity

Ingestion measurements were carried out within the disk cavity at three axial positions (x/s =0.09091, 0.39394, 0.69697, 1; s=16.5 mm) at three specific radial locations (r =179 mm, 148 mm, 104 mm) for three purge gas flow rates (c_w = 770, 1540, 3080). Measurements at the other radial locations and purge gas flow rates were not performed as the ingestion measurements within the cavity were quite time consuming.

From figure 3.13, experiment set I condition, it can be observed that for c_w =770 and 1540 the main stream gas ingestion is maximum at the stator disk and minimum near the rotor in the rim cavity. This is caused by the strong radial outflow of purge gas near the rotor disk, this impeding the ingested main gas from reaching the rotor disk. For c_w = 3080 the sealing effectiveness seems to be constant throughout the rim cavity because of good mixing of the ingested gas with purge air. Similar trends are found for experiment set II conditions as shown in figure 3.14.

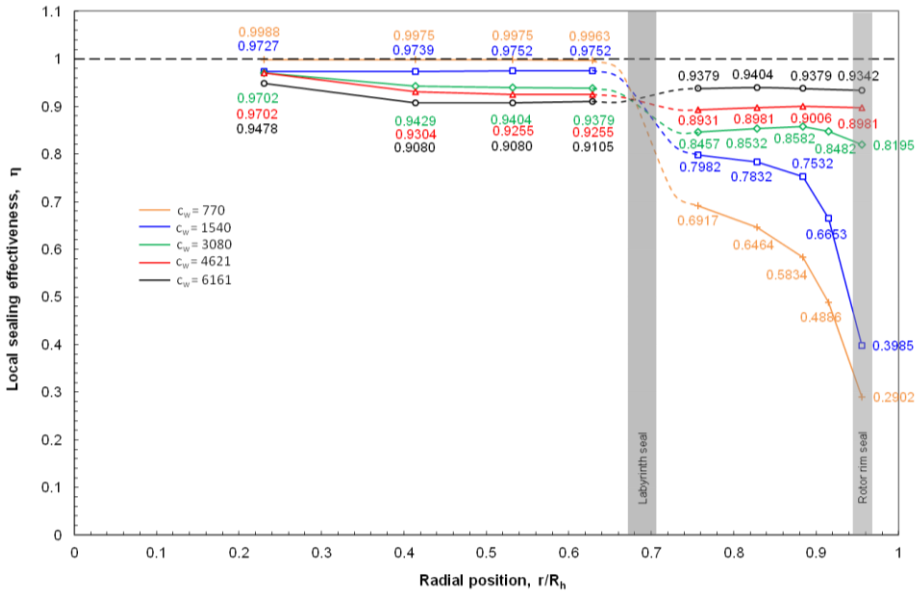

Fig 3.11 Effect of c_w on the radial distributions of sealing effectiveness in the disk cavity at the stator disk- $Re_{vax}= 1.12\times10^5$, $Re_{\varphi}= 6.14\times10^5$.

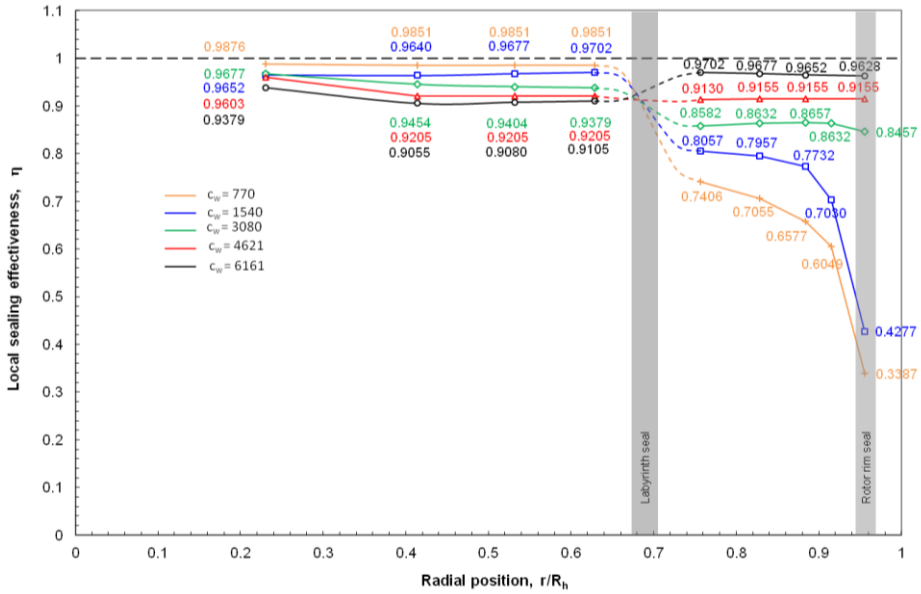

Fig 3.12 Effect of c_w on the radial distributions of sealing effectiveness in the disk cavity at the stator disk- $Re_{vax}= 9.27\times10^4$, $Re_{\varphi}=4.85\times10^5$.

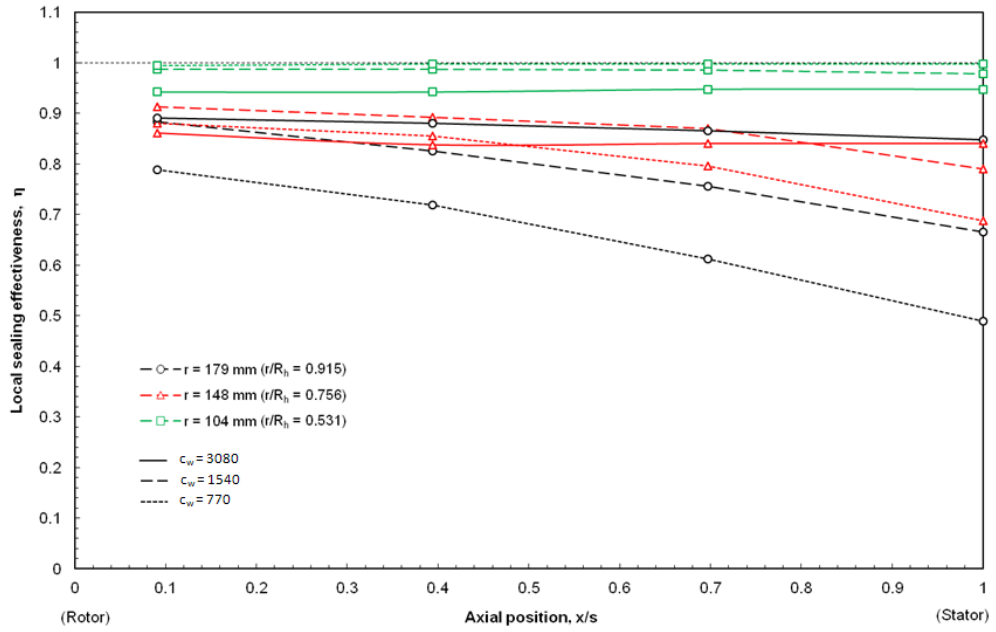

Fig 3.13 Effect of c_w on the radial distributions of sealing effectiveness within the rim-cavity- $Re_{vax}= 1.12\times10^5$, $Re_{\varphi}= 6.14\times10^5$.

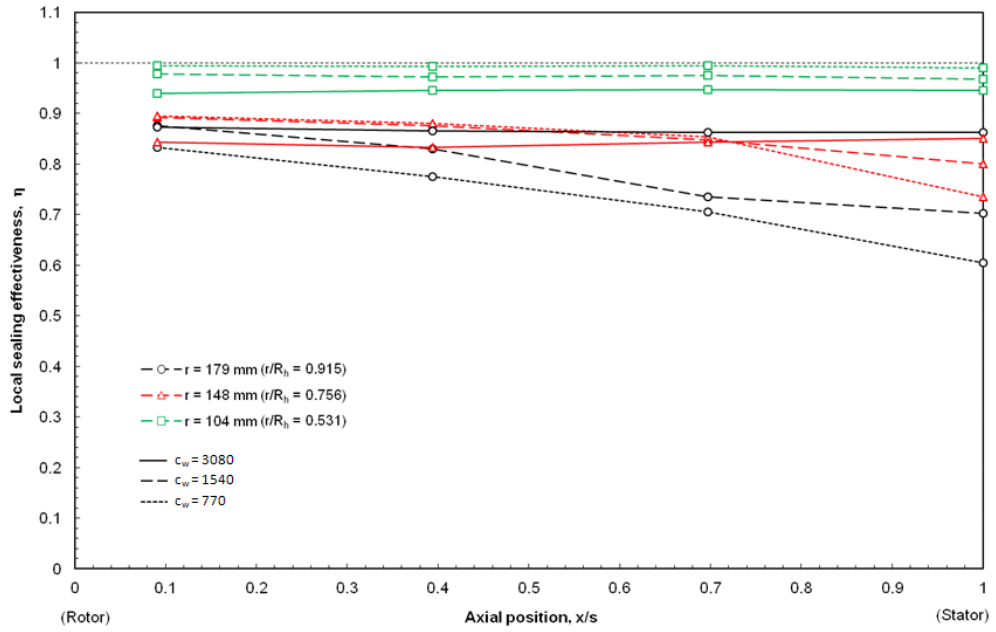

Fig 3.14 Effect of c_w on the radial distributions of sealing effectiveness within the rim-cavity- $Re_{vax}= 9.27\times10^4$, $Re_{\varphi}= 4.85\times10^5$.

3.4 Relating the measured ingestion distributions to the velocity field.

The velocity field in the disk cavity was mapped using Particle Image Velocimetry (PIV) to help understand the flow in the presence of substantial as well as minimal main gas ingestion. The PIV technique used and the flow field results obtained for the current rotor-stator geometry are reported in Pathak (2013).

Figures 3.15 through 3.17 contain the radial velocities obtained from the instantaneous velocity vector maps in the cavity, 4 mm from the rotor surface for Re_{vax}= 1.12×10^5, Re_{φ}=6.14×10^5, and c_w =1540, 3080, 4621. It can be observed from these plots that near the stator inner seal the radial velocity tends to be negative, its magnitude increasing with c_w. Comparing these figures with the sealing effectiveness plots one may suggest that as the purge air flow rate is increased some amount of rim cavity gas mixture is getting transported into the inner cavity, which results in a decreased sealing effectiveness in the inner cavity.or higher sealing air flow rate. As stated earlier, this result was experimentally repeatable. As suggested, this transport of the rim cavity gas mixture into the inner cavity might be due to the possible unsteady pressure structures in the inner cavity.

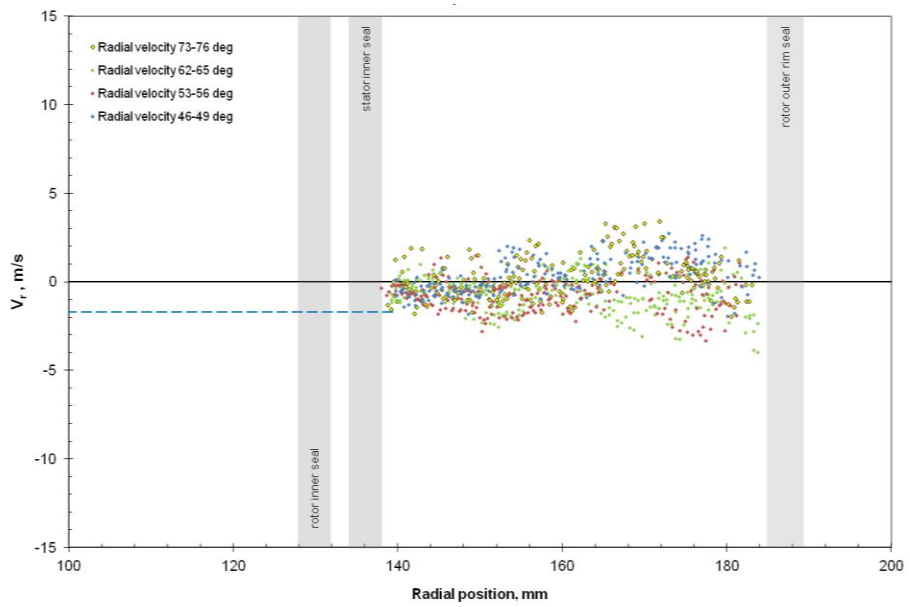

Fig 3.15 Fluid radial velocity from instantaneous velocity vector maps at four circumferential sector in the cavity; 4 mm from the rotor surface – $Re_{vax}= 1.12\times10^5$, $Re_{\varphi}= 6.14\times10^5$, $c_w = 1540$.

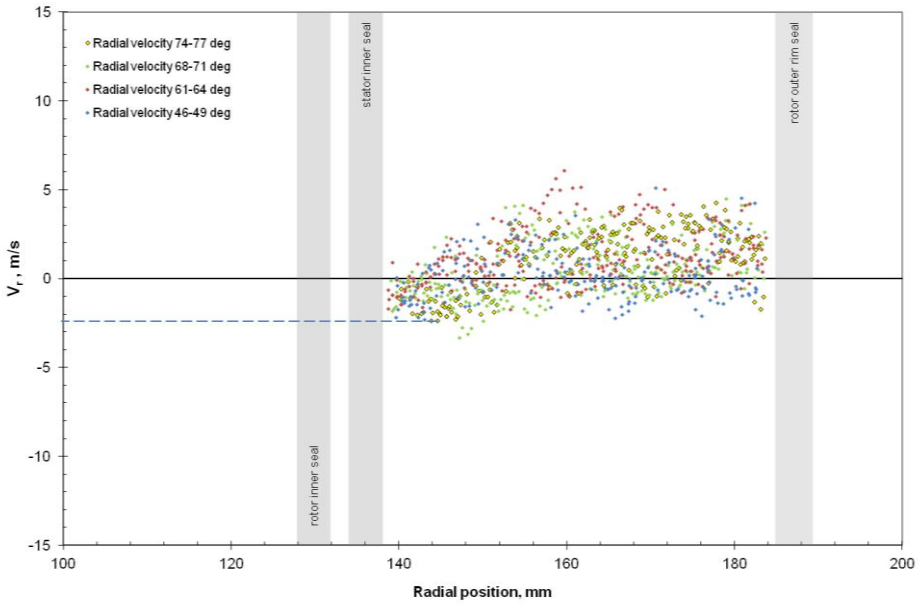

Fig 3.16 Fluid radial velocity from instantaneous velocity vector maps at four circumferential sector in the cavity; 4 mm from the rotor surface - $Re_{vax}= 1.12\times10^5$, $Re_{\varphi}= 6.14\times10^5$, $c_w = 3080$.

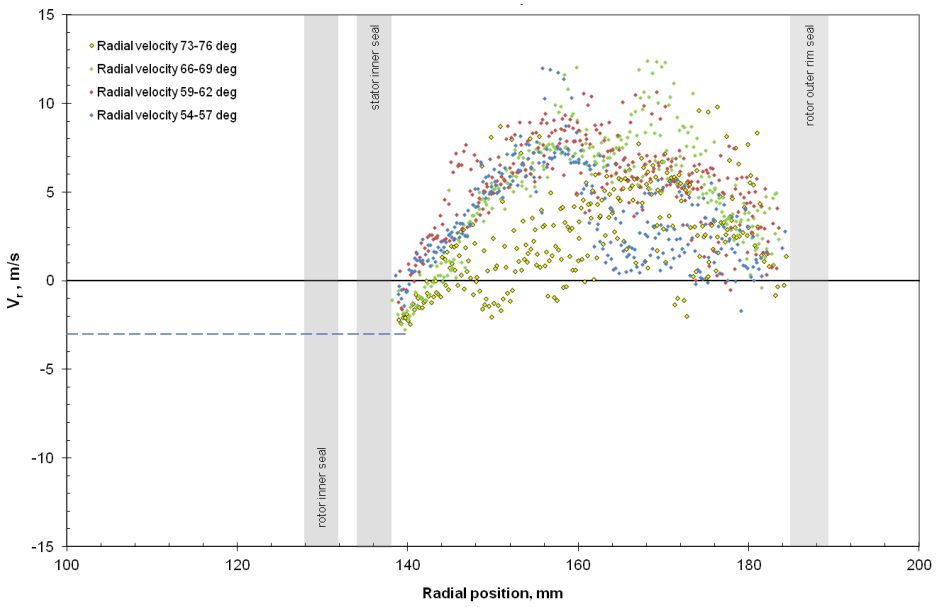

Fig 3.17 Fluid radial velocity from instantaneous velocity vector maps at four circumferential sector in the cavity; 4 mm from the rotor surface - $Re_{vax}= 1.12\times10^5$, $Re_{\varphi}= 6.14\times10^5$, $c_w = 4621$.

CHAPTER 4

CONCLUDING REMARKS AND RECOMMENDATIONS FOR FUTURE WORK

4.1 Concluding remarks

An experimental study of the time-average static pressure and the main gas ingestion distributions in a model single-stage axial flow gas turbine has been reported. The turbine stage featured vanes, blades, and rim seal on both the rotor and stator. Additionally, the disk cavity contained a labyrinth seal radially in-board which effectively divided the cavity into a *rim cavity* and an *inner cavity*.

A time-average static pressure distribution that was circumferentially-periodic following the vane pitch was found in the main gas path. The peak-to-peak amplitude of this asymmetry increased as the square of the main gas flow rate. The amplitude was the highest at the main gas path outer shroud at the vane trailing edge plane. It decayed rapidly downstream toward the rotor blades; it also decreased radially inward toward the cavity rim seal. Both the purge air exiting from the disk cavity through the rim seal clearance and the rotor blades affected the pressure decay. In the rim cavity, no circumferential pressure variation was found even at the outermost radial location of measurement, implying that the asymmetry dissipated across the rim seals.

Main gas ingestion sealing effectiveness distribution was measured both at the stator disk surface and across the disk cavity. The sealing effectiveness was found to decrease as the circumferential pressure asymmetry in the main gas path

increased with increase in the main gas flow rate. In the rim cavity, the sealing effectiveness depended strongly on the purge air flow rate, increasing as the flow rate increased. However, the sealing effectiveness in the inner cavity was found to decrease somewhat as the purge air flow rate increased. This may have been due to unsteady low-pressure structures that could have existed in the outermost region of the inner cavity. Disk pumping by the rotor disk is also known to influence ingestion, a higher rotor speed tending to increase ingestion (i.e. decrease sealing effectiveness).

The sealing effectiveness near the rotor disk was generally found to be higher than near the stator, meaning that ingestion was higher in the vicinity of the stator.

4.2 Recommendations for future work

Rim seal geometry is one of the factors that influence the rim cavity pressure distribution and thus influences the main gas ingestion. It would be useful to study the influences of rim seal geometry parameters such as radial clearance and axial overlap on main gas ingestion. Different rim cavity aspect ratios, which can be obtained by changing the radial location of the labyrinth seal, should also be studied.

In the current disk cavity configuration, the labyrinth seal separates the inner cavity from the rim cavity. Recent experiments in our laboratory indicate that the clearance provided in the seal is a sensitive parameter, both for the cavity

pressure distribution and the cavity sealing effectiveness distribution. Additional experiments will be needed to properly understand this issue.

In addition to the time-averaged pressure measurement, unsteady instantaneous pressure measurements also need to be carried out. As has been reported in various published works, it is the instantaneous differential between the main gas path and rim cavity pressures that drives ingestion. The measurements reported in this thesis are time-averaged pressure (averaged over many rotor revolutions). Measurement of the instantaneous pressure at the stator rim seal (vane platform) tip, outer shroud and within the rim cavity would allow us to better understand the mechanism of main gas ingestion.

At the time of writing this thesis three-dimensional unsteady CFD is being carried out. Its results are expected to augment the experimental results reported.

REFERENCES

Abe, T., Kikuchi, J., and Takeuchi, H., 1979, "An Investigation of Turbine Disk and Cooling," 13th CIMAC Congress, Vienna.

Bohn, D. E., Decker, A., and Ohlendorf, N., 2006, "Influence of Radial and Axial Rim Seal Geometry on Hot Gas Ingestion into the Upstream Cavity of a 1.5 Stage Turbine", ASME Paper No. GT2006-90453.

Cao, C., Chew, J.W., Millington, P.R., and Hogg, S.I., 2003, "Interaction of Rim Seal and Annulus Flows in an Axial Flow Turbine," ASME Paper GT-2003-38368.

Chew, J. W. (1991). "A Theoretical Study of Ingress for Shrouded Rotating Disk Systems With Radial Outflow." ASME J. Turbomach. 113(1): pp. 91-97.

Gentilhomme, O., Hills, N.J., Chew, J.W., and Turner, A.B., 2002, "Measurement and Analysis of Ingestion through a Turbine Rim Seal," ASME Paper GT-2002-30481.

Green, T. and Turner, A. B., 1994, "Ingestion into the Upstream Wheelspace of an Axial Turbine Stage," *ASME Journal of Turbomachinery*, Vol. 116, pp. 327-332.

Hamabe, K., and Ishida, K., 1992, "Rim Seal Experiments and Analysis of a Rotor-Stator System with Nonaxisymmetric Main flow," ASME Paper 92-GT-160.

Jakoby, R., Zierer, T., Klas, L., and Larsson, J., deVito, L., Bohn, E. D., Funcke, J and Decker, A., 2004, "Numerical simulation of the Unsteady Flow Field in an Axial Gas Turbine Rim Seal Configuration," ASME Paper GT2004-53829.

Johnson, B.V., Mack, G.J., Paolillo, R.E., and Daniels, W.A., 1994, "Turbine Rim Seal Gas Path Flow Ingestion Mechanisms," AIAA Paper 94-2703.

Johnson, B. V., Wang, C. Z. and Roy, R. P. (2008). A Rim Seal Orifice Model with 2 Cd s and Effects of Swirl in Seals. ASME Paper GT2008-50650

Owen, J.M. and Rogers, R.H., 1989, Flow and Heat Transfer in Rotating-Disc Systems. Vol. I: Rotor-Stator Systems, Research Studies Press, Taunton, United Kingdom.

Pathak, P.S., 2013, “Experimental Study of Flow Field in a Model Rotor-Stator Disk Cavity Using Particle Image Velocimetry”, M.S., Thesis, Arizona State University.

Phadke, U. P. and Owen, J. M. (1983). "An Invesigation Of Ingress For An Air-Cooled Shrouded Rotating-Disk System With Radial-Clearance Seals." Journal of Engineering for Power-Transactions of the ASME 105(1): pp. 178-183.

Phadke, U. P. and Owen, J. M., 1988, “Aerodynamic Aspects of the Sealing of Gas-Turbine Rotor-Stator Systems, Part 3: The Effect of Nonaxisymmetric External Flow on Seal Performance,” *International Journal of Heat and Fluid Flow*, Vol. 9(2), pp. 113-117.

Rolls-Royce, 1986, The Jet Engine, Key Publishing Limited, Stamford, United Kingdom.

Roy, R.P., Devasenathipathy, S., Xu, G., and Zhao, Y., 1999, “A Study of the Flow Field in a Model Rotor-Stator Disk Cavity”, ASME Paper 99-GT-246.

Roy, R.P., Xu, G., and Feng, J., 2000, “Study of Main-Stream Gas Ingestion in a Rotor-Stator Disk Cavity”, AIAA Paper 2000-3372.

Roy, R.P., Feng, J., Narzary, D., and Paolollo, R.E., 2005, “Experiment on Gas Ingestion Through Axial-Flow Turbine Rim Seals”, ASME *Journal of Engineering for Gas Turbines and Power*, Vol. 127. 127, pp.573-582.

Roy, R.P., Zhou, D.W., Ganesan, S., Wang, C-Z., Paolollo, R.E., and Johnson, B.V., 2007, “The Flow Field and Main Gas Ingestion in a Rotor-Stator Cavity”, ASME Paper GT2007-27671.

Zhou, D.W., Roy, R.P., Wang, C.Z., and Glahn, G.A., 2011, “Main gas Ingestion in a Turbine Stage for Three rim Cavity Configurations”, ASME Journal of Turbomachinary, Vol. 133, pp. 031023-1- 031023-12.

APPENDIX A

MEASUREMENT UNCERTAINTY

MEASUREMENT UNCERTAINTY

Every measurement is subject to some uncertainty. A measurement result is only complete if it is accompanied by a statement of the uncertainty in the measurement. Measurement uncertainties can arise from the measuring instrument, from the variable being measured, from the environment, from the measurer, as well as from other sources.

Each measurement error will combine in some manner with other errors to increase the uncertainty of the measurement. Each individual error is referred to as an element of error. Consider a measurement of x which is subjected to, say, K elements of error, e_j, where j=1, 2… K. A realistic estimate of the uncertainty in the measurement, u_x, due to these elemental errors can be computed using the root-sum-squares method (RSS).

$$u_x = \pm\sqrt{e_1^2 + e_2^2 + \cdots + e_K^2} \qquad (A.1)$$

$$u_x = \pm\sqrt{\sum_{j=1}^{K} e_j^2} \qquad (A.2)$$

Uncertainty in time-average static gage pressure measurement

As mentioned in Chapter-2, the time-average static pressure is measured using a variable reluctance transducer (DP-45), which is routed to the data acquisition system (DATA6500- Analogic) via a pressure signal carrier demodulator (CD-12).

The uncertainty in the measured pressure arises due to the accuracy of the combined system of variable reluctance transducer (DP-45) & pressure signal carrier demodulator (CD-12) and uncertainty in the data acquisition system as shown below in figure A.1.

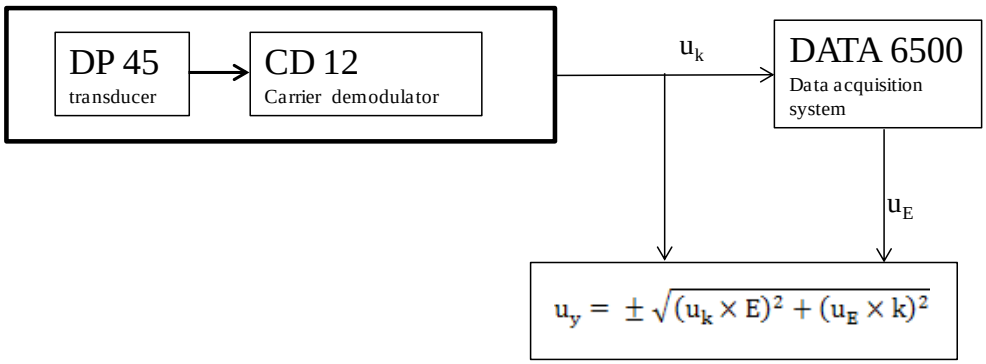

Fig A.1 Sources of uncertainty in the measured pressure

Following is the pressure transducer calibration equation

$$y = k \times E \qquad (A.3)$$

y is the measured pressure (psi)

E is the measured voltage (volts)

k is the calibration constant (psi/V)

Therefore the overall uncertainty in the measured pressure (u_y) can be written as

$$u_y = f(u_E, u_k) \qquad (A.4)$$

u_E=uncertainty in the measured voltage (volts)

u_k=uncertainty in the calibration constant (psi/V)

$$u_y = \pm\sqrt{(\theta_k \times u_k)^2 + (\theta_E \times u_E)^2} \qquad (A.5)$$

$$\theta_k = \frac{\partial y}{\partial k} = E \tag{A.6a}$$

$$\theta_E = \frac{\partial y}{\partial E} = k \tag{A.6b}$$

$$u_y = \pm\sqrt{(u_k \times E)^2 + (u_E \times k)^2} \tag{A.7}$$

Estimating the uncertainty in calibration constant (u_k)

The uncertainty in k can be estimated in two different ways. The first approach makes use of the accuracy value of the pressure transducer (DP-45) quoted in the technical manual. The second approach directly uses the calibration data provided for DP45 by Validyne.

u_k based on DP45's quoted accuracy

The quoted accuracy of the pressure transducer (DP-45, Validyne) is $\pm$0.25% of the FS which is 2 psi (corresponds to 10V in CD-12). Hence the uncertainty @ 2 psi measurement is $\pm$ 0.005 psi. The average value of the calibration constant, k_{avg} is 0.2 psi/volt.

So, k'=2.005 psi/ 10 volts = 0.2005 psi/volt

& k"=1.995 psi/10 volts = 0.1995 psi/volt

Therefore the uncertainty in the calibration constant estimated using the quoted accuracy of DP45 is $u_k = \pm 0.0005$ psi/volt .

u_k based on DP45 calibration data provided by Validyne

From the calibration data provided by Validyne, the value of k was calculated to be k = 0.200022 ± 0.000675 psi/V (mean ± stdev). So the uncertainty in the calibration constant can be taken as $u_k = \pm 0.000675$ psi/volt

Based on the above two estimates it was decided to use the larger value for the uncertainty in the calibration constant $u_k = \pm 0.000675$ psi/volt for calculating the overall uncertainty.

Estimating the uncertainty in the measured voltage (u_E)

The uncertainty of the voltage measured by the data acquisition system (Analogic DATA6500) depends on the quoted accuracy $(u_a)_E$ and the resolution $(u_r)_E$ of DATA6500.

$$u_E = \pm \sqrt{(u_a)_E{}^2 + (u_r)_E{}^2} \qquad (A.8)$$

Quoted accuracy = (0.05% of measured Voltage + 0.05% of input range)

Resolution = 0.6 mV. Hence $(u_r)_E = \pm 0.3$ mV

Sample uncertainty calculation for a measured pressure:

A static gage pressure of -5157.96 Pa was measured on the outer-shroud for the experimental condition $Re_{vax} = 1.12\times10^5$, $Re_\varphi = 6.14\times10^5$, $c_w = 1540$. Table A.1 shows the calculation of uncertainty for this measured pressure.

Table A.1 Calculation of uncertainty in a 'sample' measured pressure value

Symbol	Description	Values	Units	Formula
k	Calibration constant	0.200022	psi/V	----
u_k	Uncertainty in k	0.000675	psi/V	----
MP	Measured P	-5157.96	Pa	----
MP	Measured P	-0.7481	psi	----
Mv	Measured Voltage	-3.74008	V	MP/k
E	Absolute Voltage	3.74008	V	Abs(Mv)
$(u_a)_E$	Accuracy of DATA6500	0.00437	V	(0.05% of E + 0.05% of 5 V); ±5V was the input range
$(u_r)_E$	Resolution of DATA6500	0.0003	V	(Quoted resolution)/2
u_E	Uncertainty in measured voltage	0.004377	V	Equation A.8
u_y	Total uncertainty of measured P	±0.002672	psi	Equation A.7
$\%u_y$	% uncertainty in measured Pressure	±0.357181	%	

The maximum uncertainty from all the measured pressure values was found to be ± 0.364%. Thus a conservative estimate of ± 0.4% is used as the maximum uncertainty in the measured static gage pressure.

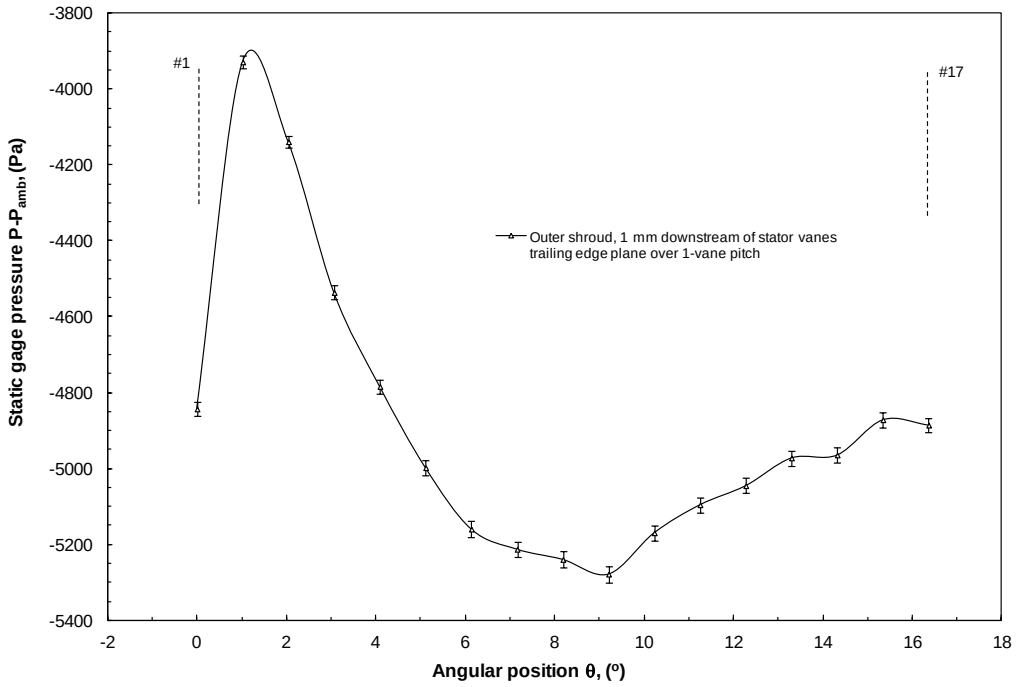

Fig A.2 Error bar representation of circumferential distribution of time-average static-gage pressure in the main gas path – Re_{vax}= 1.12×10^5, Re_{φ}= 6.14×10^5, c_w = 1540.

Figure A.2 shows the ±0.4% uncertainty in the measured value of the circumferential distribution of pressure in the main gas path on the outer shroud over one vane pitch for the experimental condition Re_{vax} = 1.12×10^5, Re_{φ} = 6.14×10^5, c_w = 1540.

Uncertainty in concentration measurements

The NDIR gas analyzer (Siemens- Ultramat 23) is calibrated using pure nitrogen and a calibration gas. During the AUTOCAL process, the chamber is purged with nitrogen gas for zero point calibration, and also serves as the initial value for calculating the full-scale value. The calibration point is also checked every 3 months using a calibration gas (4% CO_2 and 96% N_2 balance, flow rate: 1.2-1.8 l/min).

For the gas concentration measurement experiments, the CO_2 concentration in the gas sample was measured by the Siemens Ultramat 23. The various elements of errors are:

- The quoted accuracy of the gas analyzer is $\pm$2% FS (which is 5% CO_2 volumetric concentration). Thus, the uncertainty in the measured CO_2 volumetric concentration due to the accuracy of the instrument is $\pm$0.10 % CO_2 concentration.
- The repeatability error was found to be $\pm$0.5%. Since the maximum concentration measured in the experiment is 4% CO_2 volumetric concentration, the uncertainty in the measured concentration due to the repeatability error is $\pm$0.02 % CO_2 concentration.
- The precision of measurements made with a digital instrument is based predominantly on the reading uncertainty. The uncertainty in reading a digital scale is ±1/2 of the last resolvable digit. The uncertainty in the

measured CO_2 volumetric concentration due to the precision error is ± 0.005 % CO_2 concentration.

From equation A.1

$$u_x = \pm\sqrt{(0.10)^2 + (0.02)^2 + (0.005)^2}$$

$$u_x = \pm\sqrt{0.010425}$$

$$u_x = \pm 0.1021$$

Therefore the overall uncertainty in the CO_2 volumetric concentration at a measured 4% value is 4.00 ($\pm$ 0.102) %.

The CO_2 mass concentration is calculated as shown below

$$m_{CO\,2} \approx \frac{v_{CO\,2}}{0.6584 + 0.3416\, v_{CO\,2}} \qquad (A.9)$$

Where

$m_{CO\,2}$= Mass concentration of CO_2 gas

$v_{CO\,2}$= Volumetric concentration of CO_2 gas

The CO_2 mass concentration for 4% CO_2 volumetric concentration is calculated using equation A.9.

$$m_{CO\,2} \approx \frac{0.04}{0.6584 + 0.3416 \times 0.04}$$

$$m_{CO\,2} \approx 5.9518\%$$

Calculating the uncertainty in mass concentration of CO_2 gas:

$$m_{CO\,2} \approx \frac{0.04 \pm 0.00102}{0.6584 + 0.3416 \times (0.04 \pm 0.00102)}$$

$$m_{CO\,2} \approx 5.9518 \pm 0.1487\ \%$$

Therefore the overall uncertainty in the CO_2 mass concentration (at a measured 4% volumetric concentration; equivalently 5.95% mass concentration) is $\pm 0.15\%$ mass concentration.